Carbon Monitoring System Flux Net Biosphere Exchange 2020 (CMS-Flux NBE 2020)

Junjie Liu[1,2], **Latha Baskaran**[1], **Kevin Bowman**[1], **David Schimel**[1], **A. Anthony Bloom**[1],
Nicholas C. Parazoo[1], **Tomohiro Oda**[3,4], **Dustin Carroll**[5], **Dimitris Menemenlis**[1], **Joanna Joiner**[6],
Roisin Commane[7], **Bruce Daube**[8], **Lucianna V. Gatti**[9], **Kathryn McKain**[10,11], **John Miller**[10],
Britton B. Stephens[12], **Colm Sweeney**[10], and **Steven Wofsy**[8]

[1]Jet Propulsion Laboratory, California Institute of Technology, Pasadena, CA, USA
[2]California Institute of Technology, Pasadena, CA, USA
[3]Global Modeling and Assimilation Office, NASA Goddard Space Flight Center, Greenbelt, USA
[4]Goddard Earth Sciences Technology and Research, Universities Space Research Association,
Columbia, MD, USA
[5]Moss Landing Marine Laboratories, San José State University, Moss Landing, CA, USA
[6]Laboratory for Atmospheric Chemistry and Dynamics, NASA Goddard Space Flight Center, Greenbelt, USA
[7]Lamont-Doherty Earth Observatory of Columbia University, Palisades, NY, USA
[8]Department of Earth and Planetary Sciences, Harvard University, Cambridge, MA, USA
[9]LaGEE, CCST, INPE – National Institute for Space Research, São José dos Campos, SP, Brazil
[10]NOAA, Global Monitoring Laboratory, Boulder, CO 80305, USA
[11]Cooperative Institute for Research in Environmental Sciences, University of Colorado, Boulder, CO, USA
[12]National Center for Atmospheric Research, Boulder, CO 80301, USA

Correspondence: Junjie Liu (junjie.liu@jpl.nasa.gov)

Abstract. Here we present a global and regionally resolved terrestrial net biosphere exchange (NBE) dataset with corresponding uncertainties between 2010–2018: Carbon Monitoring System Flux Net Biosphere Exchange 2020 (CMS-Flux NBE 2020). It is estimated using the NASA Carbon Monitoring System Flux (CMS-Flux) top-down flux inversion system that assimilates column CO_2 observations from the Greenhouse Gases Observing Satellite (GOSAT) and NASA's Observing Carbon Observatory 2 (OCO-2). The regional monthly fluxes are readily accessible as tabular files, and the gridded fluxes are available in NetCDF format. The fluxes and their uncertainties are evaluated by extensively comparing the posterior CO_2 mole fractions with CO_2 observations from aircraft and the NOAA marine boundary layer reference sites. We describe the characteristics of the dataset as the global total, regional climatological mean, and regional annual fluxes and seasonal cycles. We find that the global total fluxes of the dataset agree with atmospheric CO_2 growth observed by the surface-observation network within uncertainty. Averaged between 2010 and 2018, the tropical regions range from close to neutral in tropical South America to a net source in Africa; these contrast with the extra-tropics, which are a net sink of 2.5 ± 0.3 Gt C/year. The regional satellite-constrained NBE estimates provide a unique perspective for understanding the terrestrial biosphere carbon dynamics and monitoring changes in regional contributions to the changes of atmospheric CO_2 growth rate. The gridded and regional aggregated dataset can be accessed at https://doi.org/10.25966/4v02-c391 (Liu et al., 2020).

1 Introduction

New top-down inversion frameworks that harness satellite observations provide an important complement to global aggregated fluxes (e.g., Global Carbon Budget (GCB), Friedlingstein et al., 2019) and inversions based on surface CO_2 observations (e.g., Chevallier et al., 2010), especially over the tropics and the Southern Hemisphere (SH) where conventional surface CO_2 observations are sparse. The net biosphere exchange (NBE), which is the net carbon flux of all the land–atmosphere exchange processes except fossil fuel emissions, is far more variable and has far more uncertainty than ocean fluxes (Lovenduski and Bonan, 2017) or fossil fuel emissions (Yin et al., 2019) and is thus the focus of this dataset estimated from a top-down atmospheric CO_2 inversion of satellite column CO_2 dry-air mole fraction (X_{CO_2}). Here, we present the global and regional NBE as a series of maps, time series, and tables and disseminate it as a public dataset for further analysis and comparison to other sources of flux information. The gridded NBE dataset and its uncertainty, air–sea fluxes, and fossil fuel emissions are also available so that users can calculate the carbon budget from a regional to global scale. Finally, we provide a comprehensive evaluation of both mean and uncertainty estimates against the CO_2 observations from independent airborne datasets and the NOAA marine boundary layer (MBL) reference sites (Conway et al., 1994).

Global top-down atmospheric CO_2 flux inversions have been historically used to estimate regional terrestrial NBE. They make uses of the spatiotemporal variability of atmospheric CO_2, which is dominated by NBE, to infer net carbon exchange at the surface (Chevallier et al., 2005; Baker et al., 2006a; Liu et al., 2014). The accuracy of the NBE from top-down flux inversions is determined by the density and accuracy of the CO_2 observations, the accuracy of modeled atmospheric transport, and knowledge of the prior uncertainties of the flux inventories.

For CO_2 flux inversions based on high precision in situ and flask observations, the measurement error is low (< 0.2 ppm, parts per million) and not a significant source of error; however, these observations are limited spatially and are concentrated primarily over North America (NA) and Europe (Crowell et al., 2019). Satellite X_{CO_2} observations from CO_2-dedicated satellites, such as the Greenhouse Gases Observing Satellite (GOSAT) (launched in July 2009) and the Observing Carbon Observatory 2 (OCO-2) (Crisp et al., 2017), have much broader spatial coverage (O'Dell et al., 2018), which fills the observational gaps of conventional surface CO_2 observations, but they have up to an order of magnitude higher single-sounding uncertainty and potential systematic errors compared to the in situ and flask CO_2 observations. Recent progress in instrument error characterization, spectroscopy, and retrieval methods has significantly improved the accuracy and precision of the X_{CO_2} retrievals (O'Dell et al., 2018; Kiel et al., 2019). The single-sounding random error of X_{CO_2}

from OCO-2 is ~ 1.0 ppm (Kulawik et al., 2019). A recent study by Byrne et al. (2020) shows less than a 0.5 ppm difference between posterior X_{CO_2} constrained by a recent dataset, ACOS-GOSAT b7 X_{CO_2} retrievals, and those constrained by conventional surface CO_2 observations. Chevallier et al. (2019) also showed that an OCO-2-based flux inversion had similar performance to surface CO_2-based flux inversions when comparing posterior CO_2 mole fractions to aircraft CO_2 in the free troposphere. Results from these studies show that systematic uncertainties in CO_2 retrievals from satellites are comparable to, or smaller than, other uncertainty sources in atmospheric inversions (e.g., transport).

A newly developed biogeochemical model–data fusion system, CARDAMOM, made progress in producing NBE uncertainties, along with mean values that are consistent with a variety of observations assimilated through a Markov chain Monte Carlo (MCMC) method (Bloom et al., 2016, 2020). Transport model errors in general have also been reduced relative to earlier transport model intercomparison efforts, such as TransCom 3 (Gurney et al., 2004; Gaubert et al., 2019). Advancements in satellite retrieval, transport, and prior terrestrial biosphere modeling have led to more mature inversions constrained by satellite X_{CO_2} observations.

Two satellites, GOSAT and OCO-2, have now produced more than 10 years of observations. Here we harness the NASA Carbon Monitoring System Flux (CMS-Flux) inversion framework (Liu et al., 2014, 2017, 2018; Bowman et al., 2017) to generate an NBE product – Carbon Monitoring System Flux Net Biosphere Exchange 2020 (CMS-Flux NBE 2020) – by assimilating both GOSAT and OCO-2 from 2010–2018. The dataset is the longest satellite-constrained NBE product so far. The CMS-Flux framework exploits globally available X_{CO_2} to infer spatially resolved total surface–atmosphere exchange. In combination with constituent fluxes, e.g., gross primary production (GPP), NBE from CMS-Flux framework has been used to assess the impacts of El Niño on terrestrial biosphere fluxes (Bowman et al., 2017; Liu et al., 2017) and the role of droughts in the North American carbon balance (Liu et al., 2018). These fluxes have furthermore been ingested into land–surface data assimilation systems to quantify heterotrophic respiration (Konings et al., 2019), evaluate structural and parametric uncertainty in carbon–climate models (Quetin et al., 2020), and inform climate dynamics (Bloom et al., 2020). We present the regional NBE and its uncertainty based on three types of regional masks: (1) latitude and continent, (2) distribution of biome types (defined by plant functional types) and continent, and (3) TransCom regions (Gurney et al., 2004).

The outline of the paper is as follows: Sect. 2 describes methods, and Sects. 3 and 4 describe the dataset and the major NBE characteristics, respectively. We extensively evaluate the posterior fluxes and uncertainties by comparing the posterior CO_2 mole fractions against aircraft observations and the NOAA MBL reference CO_2, as well as a gross primary production (GPP) product (Sect. 5). In Sect. 6, we dis-

cuss the strength and weakness as well as potential usage of the data. A summary is provided in Sect. 7, and Sect. 8 describes the dataset availability and future plan.

2   Methods

2.1   CMS-Flux inversion system

The CMS-Flux framework is summarized in Fig. 1. The center of the system is the CMS-Flux inversion system, which optimizes NBE and air–sea net carbon exchanges with a 4D-Var inversion system (Liu et al., 2014). In the current system, we assume no uncertainty in fossil fuel emissions, which is a widely adopted assumption in global flux inversion systems (e.g., Crowell et al., 2019), since the uncertainty in fossil fuel emissions at regional scales is substantially less than the NBE uncertainties. The 4D-Var minimizes a cost function that includes two terms:

$$J(\boldsymbol{x}) = (\boldsymbol{x} - \boldsymbol{x}_b)^T \mathbf{B}^{-1} (\boldsymbol{x} - \boldsymbol{x}^b)$$
$$+ (\boldsymbol{y} - h(\boldsymbol{x}))^T \mathbf{R}^{-1} (\boldsymbol{y} - h(\boldsymbol{x})). \qquad (1)$$

The first term measures the differences between the optimized fluxes and the prior fluxes normalized by the prior flux error covariance $\mathbf{B}$. The second term measures the differences between observations ($\boldsymbol{y}$) and the corresponding model simulations ($h(\boldsymbol{x})$) normalized by the observation error covariance $\mathbf{R}$. The term $h(\cdot)$ is the observation operator that calculates observation-equivalent model-simulated X_{CO_2}. The 4D-Var uses the adjoint (i.e., the backward integration of the transport model) (Henze et al., 2007) of the GEOS-Chem transport model to calculate the sensitivity of the observations to surface fluxes. The configurations of the inversion system are summarized in Table 1. We run both the forward model and its adjoint at $4° \times 5°$ spatial resolution and optimize monthly NBE and air–sea carbon fluxes at each grid point from January 2010 to December 2018. Inputs for the system include prior carbon fluxes, meteorological drivers, and the satellite X_{CO_2} (Fig. 1). Sect. 2.2 (Table 2) describes the prior flux and its uncertainties, and Sect. 2.3 (Table 3) describes the observations and the corresponding uncertainties.

2.2   The prior CO_2 fluxes and uncertainties

The prior CO_2 fluxes include NBE, air–sea carbon exchange, and fossil fuel emissions (see Table 2). The data sources for the prior fluxes are listed in Table 7 and provided in the gridded fluxes. Methods to generate prior ocean carbon fluxes and fossil fuel emissions are documented in Brix et al. (2015), Caroll et al. (2020), and Oda et al. (2018). The focus of this dataset is optimized terrestrial biosphere fluxes, so we briefly describe the prior terrestrial biosphere fluxes and their uncertainties.

We construct the NBE prior using the CAR-DAMOM framework (Bloom et al., 2016). The CAR-DAMOM data assimilation system explicitly represents the

time-resolved uncertainties in the NBE. The prior estimates are already constrained with multiple data streams accounting for measurement uncertainties following a Bayesian approach similar to that used in the 4D-variational approach. We use the CARDAMOM setup as described by Bloom et al. (2016, 2020) resolved at monthly timescales; data constraints include Global Ozone Monitoring Experiment 2 (GOME-2) solar-induced fluorescence (Joiner et al., 2013), MODIS leaf area index (LAI), and biomass and soil carbon (details on the data assimilation are provided in Bloom et al., 2020). In addition, mean GPP and fire carbon emissions from 2010–2017 are constrained by FLUXCOM RS + METEO version 1 GPP (Tramontana et al., 2016; Jung et al., 2017) and GFEDv4.1s (Randerson et al., 2018), respectively, both assimilated with an uncertainty of 20 %. We use the Olsen and Randerson (2004) approach to downscale monthly GPP and respiration fluxes to 3-hourly timescales, based on ERA-Interim re-analysis of global radiation and surface temperature. Fire fluxes are downscaled using the GFEDv4.1 daily- and diurnal-scale factors on monthly emissions (Giglio et al., 2013). Posterior CARDAMOM NBE estimates are then summarized as NBE mean and standard deviation values.

The NBE from CARDAMOM shows net carbon uptake of 2.3 Gt C/year over the tropics and close to neutral in the extra-tropics (Fig. B1). The year-to-year variability (i.e., interannual variability, IAV) estimated from CARDAMOM is generally less than 0.1 g C/m²/d outside of the tropics (Fig. B1). Because of the weak interannual variability estimated by CARDAMOM, we use the same 2017 NBE prior for 2018.

CARDAMOM generates uncertainty along with the mean state. The relative uncertainty over the tropics is generally larger than 100 %, and the magnitude is between 50 % and 100 % over the extra-tropics (Fig. B2). We assume no correlation in the prior flux errors in either space or time. The temporal and spatial error correlation estimates can in principle be computed by CARDAMOM. We anticipate incorporating these error correlations in subsequent versions of this dataset.

2.3   Column CO_2 observations from GOSAT and OCO-2

We use the satellite-column CO_2 retrievals from the Atmospheric Carbon Observations from Space (ACOS) team for both GOSAT (version 7.3) and OCO-2 (version 9) (Table 3). The use of the same retrieval algorithm and validation strategy adopted by the ACOS team to process both GOSAT and OCO-2 spectra maximizes the consistency between these two datasets. Both GOSAT and OCO-2 satellites carry high-resolution spectrometers optimized to return high-precision measurements of reflected sunlight within CO_2 and O_2 absorption bands in the shortwave infrared (Crisp et al., 2012). Both satellites fly in a sun-synchronous orbit. GOSAT has a $13{:}00 \pm 0.15$ h local passing time and a 3 d ground track repeat cycle. The footprint of GOSAT is ~ 10.5 km in diam-

https://doi.org/10.5194/essd-13-299-2021
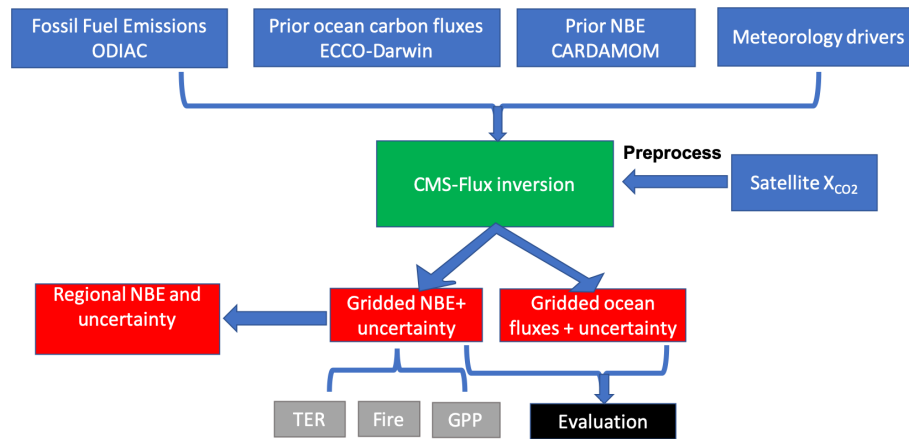
Earth Syst. Sci. Data, 13, 299–330, 2021

Figure 1. Data flow diagram with the main processing steps to generate regional net biosphere exchange (NBE). TER: total ecosystem respiration; GPP: gross primary production. The green box is the inversion system. The blue boxes are the inputs for the inversion system. The red boxes are the data outputs from the system. The black box is the evaluation step, and the gray boxes are the future additions to the product.

Table 1. Configurations of the CMS-Flux atmospheric inversion system.

	Model setup	Configuration	Reference
Inversion general setup	Spatial scale	Global	–
	Spatial resolution	4° latitude × 5° longitude	
	Time resolution	monthly	
	Minimizer of cost function	L-BFGS	Byrd et al. (1994), Zhu et al. (1997)
	Control vector	Monthly net terrestrial biosphere fluxes and ocean fluxes	
Transport model	Model name	GEOS-Chem and its adjoint	Suntharalingam et al. (2004), Nassar et al. (2010), Henze et al. (2007)
	Meteorological forcing	GEOS-5 (2010–2014) and GEOS-FP (2015–2019)	Rienecker et al. (2008)

eter in sun nadir view (Crisp et al., 2012). The daily number of soundings processed by the ACOS-GOSAT retrieval algorithm is between a few hundred to ~ 2000. Further quality control and filtering reduce the ACOS-GOSAT X_{CO_2} retrievals to ~ 100–300 daily (Fig. B5 in Liu et al., 2017). We only assimilate ACOS-GOSAT land nadir observations flagged as being good quality, which are the retrievals with quality flag equal to zero.

OCO-2 has a 13:30 local passing time and 16 d ground track repeat cycle. The nominal footprints of the OCO-2 are 1.25 km wide and ~ 2.4 km along the orbit. Because of its small footprints and sampling strategy, OCO-2 has many more X_{CO_2} retrievals than ACOS-GOSAT. To reduce the sampling error due to the resolution differences between the transport model and OCO-2 observations, we generate super observations by aggregating the observations within ~ 100 km (along the same orbit) (Liu et al., 2017). The super-obing strategy was first proposed in numerical weather prediction (NWP) to assimilate dense observations (Lorenc, 1981) and is still broadly used in NWP (e.g., Liu and Rabier, 2003). More detailed information about OCO-2 super observations can be found in Liu et al. (2017). OCO-2 has four observing modes: land nadir, land glint, ocean glint, and target. Following Liu et al. (2017), we only use land nadir observations. The super observations have more uniform spatial coverage and are more comparable to the spatial representation of ACOS-GOSAT observations and the transport model (see Fig. B5 in Liu et al., 2017).

We directly use observational uncertainty provided with ACOS-GOSAT b7.3 to represent the observation error statis-

Table 2. Description of the prior fluxes and assumed uncertainties in the inversion system.

Prior fluxes	Terrestrial biosphere fluxes	Ocean fluxes	Fossil fuel emissions
Model name	CARDAMOM-v1	ECCO-Darwin	ODIAC 2018
Spatial resolution	$4° \times 5°$	$0.5°$	$1° \times 1°$
Frequency	3-hourly	3-hourly	Hourly
Uncertainty	Estimated from CARDAMOM	100 % similar to Liu et al. (2017)	No uncertainty
References	Bloom et al. (2016, 2020)	Brix et al. (2015), Carroll et al. (2020)	Oda et al. (2018)

Table 3. Description of observation and evaluation dataset. Data sources are listed in Table 7.

	Dataset name and version	References
Satellite X_{CO_2}	ACOS-GOSAT v7.3 OCO-2 v9	O'Dell et al. (2012) O'Dell et al. (2018)
Aircraft CO_2 observations	ObsPack OCO-2 MIP HIPPO 3–5 ATom 1–4 INPE ORCAS ACT-America	CarbonTracker team (2019) Wofsy et al. (2011) Wofsy et al. (2018) Gatti et al. (2014) Stephens et al. (2017) Davis et al. (2018)
NOAA marine boundary layer (MBL) reference	NOAA MBL reference	Conway et al. (1994)
GPP	FLUXSAT GPP	Joiner et al. (2018)
Top-down NBE estimates constrained by surface CO_2	CarbonTracker Europe	van der Laan-Luijkx et al. (2017) Peters et al. (2010, 2007)
	Jena CarbonScope s10oc_v2020 CAMS v18r1	Rödenbeck et al., 2003 Chevallier et al. (2005)

tics, R, in Eq. (1). The uncertainty of the OCO-2 super observations is the sum of the variability of X_{CO_2} used to generate each individual super observation and the mean uncertainty provided in the original OCO-2 retrievals. Kulawik et al. (2019) showed that both OCO-2 and ACOS-GOSAT bias-corrected retrievals have a mean bias of -0.1 ppm when compared with X_{CO_2} from the Total Carbon Column Observing Network (TCCON) (Wunch et al., 2011), indicating consistency between ACOS-GOSAT and OCO-2 retrievals. O'Dell et al. (2018) showed that the OCO-2 X_{CO_2} land nadir retrievals have an RMSE of ~ 1.1 ppm when compared to TCCON retrievals; the differences between OCO-2 X_{CO_2} retrievals and surface-CO_2-constrained model simulations are well within 1.0 ppm over most of the locations in the Northern Hemisphere (NH), where most of the surface CO_2 observations are located.

The magnitude of observation errors used in **R** is generally above 1.0 ppm, larger than the sum of random error and biases in the observations. The ACOS-GOSAT b7.3 observations from July 2009–June 2015 are used to optimize fluxes between 2010 and 2014, and the OCO-2 X_{CO_2} observations

from September 2014–June 2019 are used to optimize fluxes between 2015 and 2018.

The observational coverage of ACOS-GOSAT and OCO-2 is spatiotemporally dependent, with more coverage during summer than winter over the NH and more observations over midlatitudes than over the tropics (Fig. B3). The variability (i.e., standard deviation) of the annual total number of observations from 2010–2014 is within 4 % of the annual mean number for ACOS-GOSAT. Except for a data gap in 2017 caused by a malfunction of the OCO-2 instrument, the variability of the annual total number of observations between 2015 and 2018 is within 8 % of the annual mean number for OCO-2.

2.4 Uncertainty quantification

The posterior flux error covariance is the inverse Hessian, which incorporates the transport, measurement, and background errors at the 4D-Var solution (Eq. 13 in Bowman et al., 2017). Posterior flux uncertainty projected to regions can be estimated analytically based on the methods described in

Fisher and Courtier (1995) and Meirink et al. (2008), using either flux singular vectors or flux increments obtained during the iterative optimization (e.g., Niwa and Fujii, 2020). In this study, we rely on a Monte Carlo approach to quantify posterior flux uncertainties following Chevallier et al. (2010) and Liu et al. (2014), which is simpler and widely used. In this approach, an ensemble of flux inversions is carried out with an ensemble of priors and simulated observations to sample the uncertainties of prior fluxes (i.e., $\mathbf{B}$ in Eq. 1) and observations ($\mathbf{R}$ in Eq. 1), respectively. The magnitude of posterior flux uncertainties is a function of assumed uncertainties in prior fluxes and observations, as well as the density of observations. Since the densities of GOSAT and OCO-2 observations are stable (Sect. 2.3) within their respective data record, we characterize the posterior flux uncertainties for 2010 and 2015 only and assume the flux uncertainties for 2011–2014 are the same as 2010 and flux uncertainties for 2016–2018 are the same as 2015.

2.5   Evaluation of posterior fluxes

Direct NBE estimates from flux towers only provide a spatial representation of roughly 1–3 km (Running et al., 1999), which is not appropriate to evaluate regional NBE from top-down flux inversions. Thus, we use two methods to indirectly evaluate the posterior NBE and its uncertainties. One is to compare annual NBE anomalies and seasonal cycle to a gross primary production (GPP) product. The other is to compare posterior CO_2 mole fractions to independent (i.e., not assimilated in the inversion) aircraft and the NOAA MBL reference observations. The second method has been broadly used to indirectly evaluate posterior fluxes from top-down flux inversions (e.g., Stephens et al., 2007; Liu and Bowman, 2016; Chevallier et al., 2019; Crowell et al., 2019). In addition to these two methods, we also compare the NBE seasonal cycles to three publicly available top-down NBE estimates that are constrained by surface CO_2 observations (Tables 3 and 7).

2.5.1   Evaluation against the independent gross primary production (GPP) product

NBE is a small residual difference between two large terms: total ecosystem respiration (TER) and GPP, plus fire. A positive NBE anomaly (i.e., less uptake from the atmosphere) has been shown to correspond to reduced GPP caused by climate anomalies (e.g., Bastos et al., 2018), and the magnitude of net uptake is proportional to GPP in most biomes observed by flux tower observations (e.g., Falk et al., 2008). Since NBE is related not only to GPP, the comparison to GPP only serves as a qualitative measure of the NBE quality. For example, we would expect the posterior NBE seasonality to be anti-correlated with GPP in the temperate and high latitudes. In this study, we use FLUXSAT GPP (Joiner et al., 2018), which is an upscaled GPP product based on
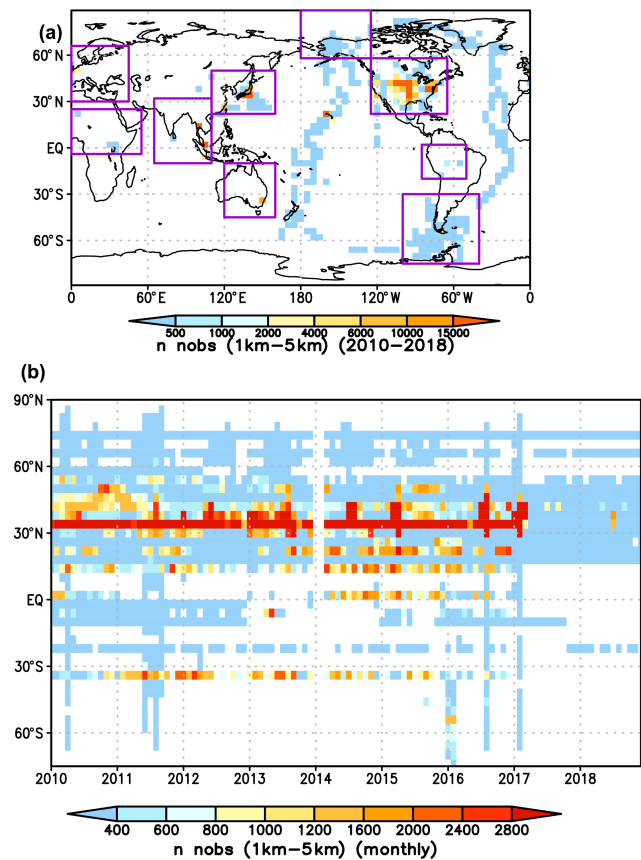

Figure 2. The spatial and temporal distributions of aircraft observations used in evaluation of posterior NBE. **(a)** The total number of aircraft observations between 1–5 km between 2010–2018 at each $4° \times 5°$ grid point. The rectangle boxes show the range of the nine sub-regions. **(b)** The total number of monthly aircraft observations at each longitude as a function of time.

flux tower GPP observations and satellite-based geometry-adjusted reflectance from the Moderate Resolution Imaging Spectroradiometer (MODIS) and solar-induced chlorophyll fluorescence observations from GOME-2 (Joiner et al., 2013). Joiner et al. (2018) show that the agreement between FLUXSAT GPP and GPP from flux towers is better than other available upscaled GPP products.

2.5.2   Evaluation against aircraft and the NOAA marine boundary layer (MBL) reference CO_2 observations

The aircraft observations used in this study include those published in OCO-2 MIP ObsPack in August 2019 (CarbonTracker team, 2019), which include regular vertical profiles from flask samples collected on light aircraft by NOAA (Sweeney et al., 2015) and other laboratories, regular (2- to 4-weekly) vertical profiles from the Instituto de Pesquisas Espaciais (INPE) over tropical South America (SA) (Gatti et al., 2014), and vertical profiles from the Atmospheric Tomography (ATom, Wofsy et al., 2018), HIAPER Pole-to-Pole Ob-

servations (HIPPO, Wofsy et al., 2011), the O_2/N_2 Ratio and CO_2 airborne Southern Ocean Study (ORCAS) (Stephens et al., 2017), and Atmospheric Carbon and Transport – America (ACT-America, Davis et al., 2018) aircraft campaigns (Table 3). Figure 2 shows the aircraft observation coverage and density between 2010 and 2018. Most of the aircraft observations are concentrated over NA. ATom had four (1–4) campaigns between August 2016 and May 2018, spanning four seasons over the Pacific and Atlantic Ocean. HIPPO had five (HIPPO 1–5) campaigns over the Pacific, but only HIPPO 3–5 occurred between 2010 and 2011. HIPPO 1–2 occurred in 2009. Based on the spatial distribution of aircraft observations, we divide the comparison into nine regions: Alaska, midlatitude NA, Europe, East Asia, South Asia, Africa, Australia, Southern Ocean, and South America (Table 4 and Fig. 2).

We calculate several quantities to evaluate the posterior fluxes and their uncertainty with aircraft observations. One is the monthly mean differences between posterior and aircraft CO_2 mole fractions. The second is the monthly root mean square errors (RMSEs) over each of the nine sub-regions, which is defined as

$$\text{RMSE} = \left(\frac{1}{n} \sum_{i=1}^{n} (y_{\text{aircraft}}^{o} - y_{\text{aircraft}}^{b})_i^2 \right)^{\frac{1}{2}}, \tag{2}$$

where y_{aircraft}^{o} is the ith aircraft observation, y_{aircraft}^{b} is the corresponding posterior CO_2 mole fraction sampled at the ith aircraft location, and n is the number of aircraft observations over each region. The RMSE is computed over the n aircraft observations within one of the nine sub-regions. The mean differences indicate the magnitude of the mean posterior CO_2 bias, while the RMSE includes both random and systematic errors in posterior CO_2. The bias and RMSE could be due to errors in posterior fluxes, transport, and initial CO_2 concentrations. When errors in transport and initial CO_2 concentrations are smaller than the errors in the posterior fluxes, the magnitude of biases and RMSE indicates the accuracy of the posterior fluxes.

To evaluate the magnitude of posterior flux uncertainty estimates, we compare RMSE against the standard deviation of ensemble simulated aircraft observations (Eq. 3) from the Monte Carlo method (RMSE_{MC}). The quantity RMSE_{MC} can be written as

$$\text{RMSE}_{\text{MC}} = \left[\frac{1}{n\text{ens}} \sum_{i\text{ens}=1}^{n\text{ens}} ((y_{\text{aircraft}}^{b(\text{MC})})_{i\text{ens}} - \bar{y}_{\text{aircraft}}^{b(\text{MC})})^2 \right]^{\frac{1}{2}}. \tag{3}$$

The variable $(y_{\text{aircraft}}^{b(\text{MC})})_{i\text{ens}}$ is the ith ensemble member of simulated aircraft observations from the Monte Carlo ensemble simulations, $\bar{y}_{\text{aircraft}}^{b(\text{MC})}$ is the mean, and $n\text{ens}$ is the total number of ensemble members. For simplicity, in Eq. (3), we drop the indices for the aircraft observations used in Eq. (2). In the absence of errors in transport and initial CO_2 concentrations,

when the estimated posterior flux uncertainty reflects the *true* posterior flux uncertainty, we show in the Appendix that

$$\text{RMSE}^2 = \frac{1}{n} \sum_{i=1}^{n} R_{i,i} + \text{RMSE}_{\text{MC}}^2, \tag{4}$$

where R_{aircraft} is the aircraft observation error variance, which could be neglected on a regional scale.

We further calculate the ratio r between RMSE and RMSE_{MC}:

$$r = \frac{\text{RMSE}}{\text{RMSE}_{\text{MC}}}. \tag{5}$$

A ratio close to one indicates that the posterior flux uncertainty reflects the true uncertainty in the posterior fluxes when the transport errors are small.

The presence of transport errors will make the comparison between RMSE and RMSE_{MC} potentially difficult to interpret. Even when RMSE_{MC} represents the actual uncertainty in posterior fluxes, the RMSE could be larger than RMSE_{MC}, since the differences between aircraft observations and model-simulated posterior mole fraction RMSE could be due to errors in both transport and the posterior fluxes, while RMSE_{MC} only reflects the impact of posterior flux uncertainty on simulated aircraft observations. In this study, we assume the primary sources of RMSE come from errors in posterior fluxes.

The RMSE and RMSE_{MC} comparison only shows differences in CO_2 space. We further calculate the sensitivity of the RMSE to the posterior flux using the GEOS-Chem adjoint. We first define a cost function J as

$$J = \text{RMSE}^2. \tag{6}$$

The sensitivity of the mean-square error to a flux, x, at location i and month j is

$$w_{i,j} = \frac{\partial J}{\partial x_{i,j}} \times x_{i,j}. \tag{7}$$

This sensitivity is normalized by the flux magnitude. Equation (7) can be interpreted as the sensitivity of the RMSE^2 to a fractional change in the fluxes. We can estimate the time-integrated magnitude of the sensitivity over the entire assimilation window by calculating

$$S_i = \frac{\sum_{j=1}^{M} |w_{i,j}|}{\sum_{k=1}^{P} \sum_{j=1}^{M} |w_{k,j}|}, \tag{8}$$

where P is the total number of grid points and M is the total number of months from the time of the aircraft data to the beginning of the inversion. The numerator of Eq. (8) quantifies the absolute total sensitivity of the RMSE^2 to the fluxes at the

https://doi.org/10.5194/essd-13-299-2021

Earth Syst. Sci. Data, 13, 299–330, 2021

Table 4. Latitude and longitude ranges for seven sub-regions.

Region	Alaska	Midlatitude NA	Europe	East Asia	South Asia
Longitude range	180–125° W	125–65° W	5° W–45° E	110–160° E	65–110° E
Latitude range	58–89° N	22–58° N	30–66° N	22–50° N	10° S–32° N
Region	Africa	South America	Australia	Southern Ocean	
Longitude range	5° W–55° E	95–50° W	120–160° E	110° W–40° E	
Latitude range	2–18° N	20° S–2° N	45–10° S	80–30° S	

ith grid. Normalized by the total absolute sensitivity across the globe, the quantity S_i indicates the relative sensitivity of RMSE^2 to fluxes at the ith grid point. Note that S_i is unitless, and it only quantifies sensitivity, not the contribution of fluxes at each grid to RMSE^2.

We use the NOAA MBL reference dataset (Table 7) to evaluate the CO_2 seasonal cycle over four latitude bands: 90–60° N, 60–20° N, 20° N–20° S, and 20–90° S. The MBL reference is based on a subset of sites from the NOAA Cooperative Global Air Sampling Network. Only measurements that are representative of a large of volume air over a broad region are considered. In the comparison, we first remove the global mean CO_2 (https://www.esrl.noaa.gov/gmd/ccgg/trends/global.html, last access: 19 May 2020) from both the NOAA MBL reference and the posterior CO_2.

2.6 Regional masks

We provide posterior NBE from 2010–2018 using three sets of regional masks (Fig. 3), in addition to the gridded product. The regional mask in Fig. 3a is based on a combination of seven plant function types condensed from MODIS IGBP and the TransCom 3 regions (Gurney et al., 2004), which is referred to as Region Mask 1 (RM1) in the following description. There are 28 regions in Fig. 3a: six in NA, four in SA, five in Eurasia (north of 40° N), three in tropical Asia, three in Australia, and seven in Africa. The regional mask in Fig. 3b is based on latitude and continents with 13 regions in total, which is referred to as Region Mask 2 (RM2) in later description. Figure 3c is the TransCom regional mask with 11 regions on land.

3 Dataset description

We present the fluxes as globally, latitudinally, and regionally aggregated time series. We show the 9-year average fluxes aggregated into RM1, RM2, and TransCom regions (Fig. 3). The aggregations are geographic (latitude and continent) and bio-climatic (biome by continent). For each region in the geographic and biome aggregations, we show 9-year mean annual net fluxes and uncertainties and then the annual fluxes for each region as a set of time-series plots. The month-by-month fluxes and uncertainties are available in tabular format, so the actual aggregated fluxes may be readily

compared to bottom-up extrapolated fluxes and Earth system models. Users can also aggregate the gridded fluxes and uncertainties based on their own defined regional masks. Table 5 provides a complete list of all data products available in the dataset. In Sect. 4, we describe the major characteristics of the dataset.

4 Characteristics of the dataset

4.1 Global fluxes

The annual atmospheric CO_2 growth rate, which is the net difference between fossil fuel emissions and total annual sink over land and ocean, is well observed by the NOAA surface CO_2 observing network (https://www.esrl.noaa.gov/gmd/ccgg/ggrn.php, last access: 12 March 2020). We compare the global total flux estimates constrained by GOSAT and OCO-2 with the NOAA CO_2 growth rate from 2010–2018 and discuss the mean carbon sink over land and ocean. Over these 9 years, the satellite-constrained atmospheric CO_2 growth rate agrees with the NOAA observed CO_2 growth rate within the uncertainty of the posterior fluxes (Fig. 4). The mean annual global surface CO_2 fluxes (in Gt C/yr) are derived from the NOAA observed CO_2 growth rate (in ppm/yr) using a conversion factor of 2.124 Gt C/ppm (Le Quéré et al., 2018). The estimated growth rate has the largest discrepancy with the NOAA observed growth rate in 2014, which may be due to a failure of one of the two solar paddles of GOSAT in May 2014 (Kuze et al., 2016). Over the 9 years, the estimated total accumulated carbon in the atmosphere is 41.5 ± 2.4 Gt C, which is slightly lower than the accumulated carbon based on the NOAA CO_2 growth rate (45.2 ± 0.4 Gt C). On average, we estimate that the NBE is 2.0 ± 0.7 Gt C, $\sim 20 \pm 8$ % of fossil fuel emissions, and the ocean sink is 3.0 ± 0.1 Gt C, $\sim 30 \pm 1$ % of fossil fuel emissions (Fig. 4). These numbers are within the ranges of the corresponding GCB estimates from Freidlingstein et al. (2019) (referred to as GCB-2019 hereafter). The mean NBE and ocean sink from GCB-2019 are 2.0 ± 1.0 Gt C and 2.5 ± 0.5 Gt C, respectively, which are 21 ± 10 % and 26 ± 5 % of fossil fuel emissions, respectively, between 2010–2018. The GCB does not report NBE directly, we calculate NBE from GCB-2019 as the residual differences between fossil fuel emissions, ocean net carbon sink, and atmospheric CO_2 growth rate. It is also equivalent to ($S_{LAND} + B_{IM} - E_{LUC}$)
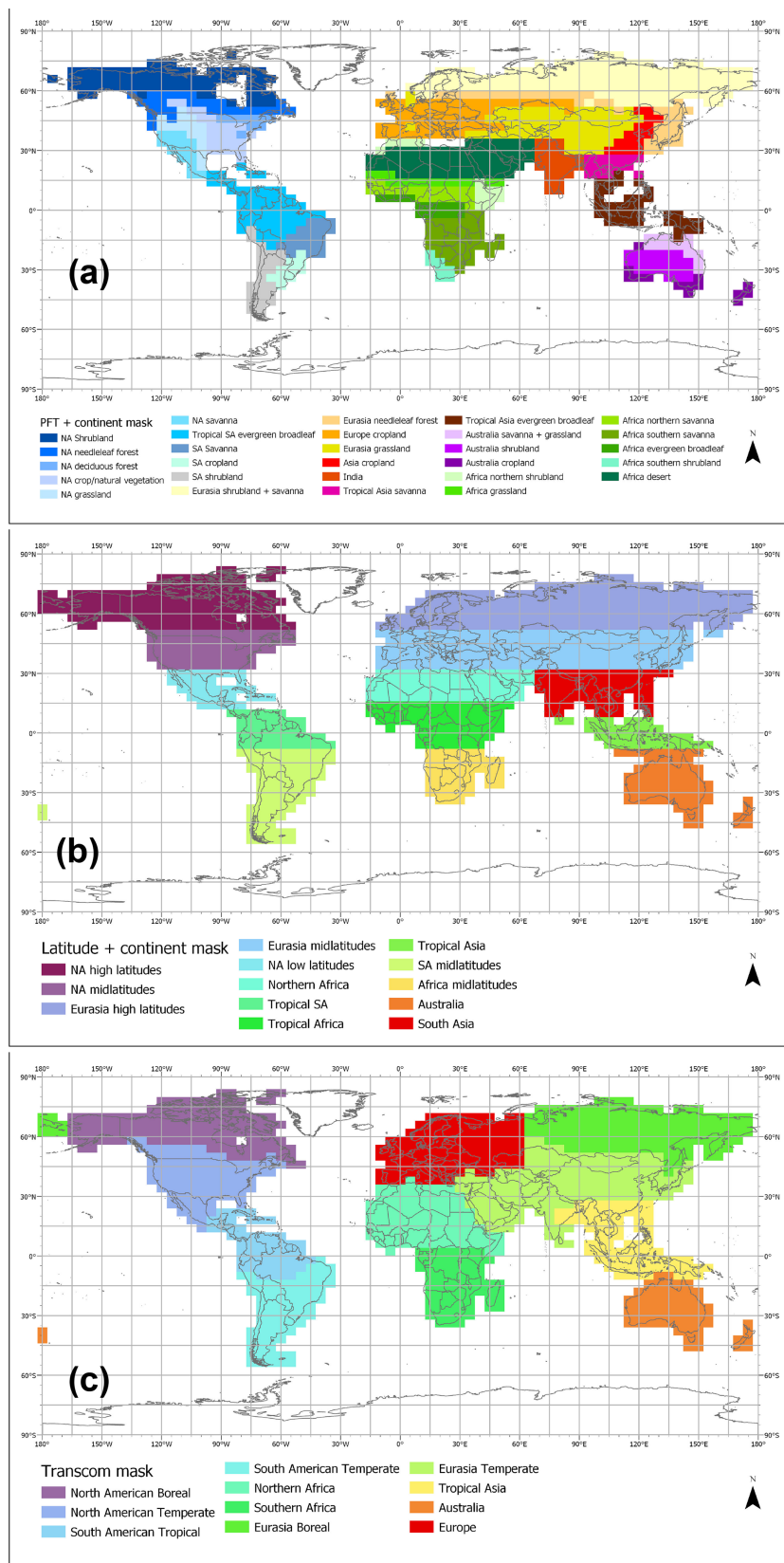
Figure 3. Three types of regional masks used in calculating regional fluxes. **(a)** The mask is based on a combination of seven condensed MODIS IGBP plant functional types, TransCom 3 regions (Gurney et al., 2004), and continents. **(b)** The mask is based on latitude and continents. **(c)** The TransCom region mask.
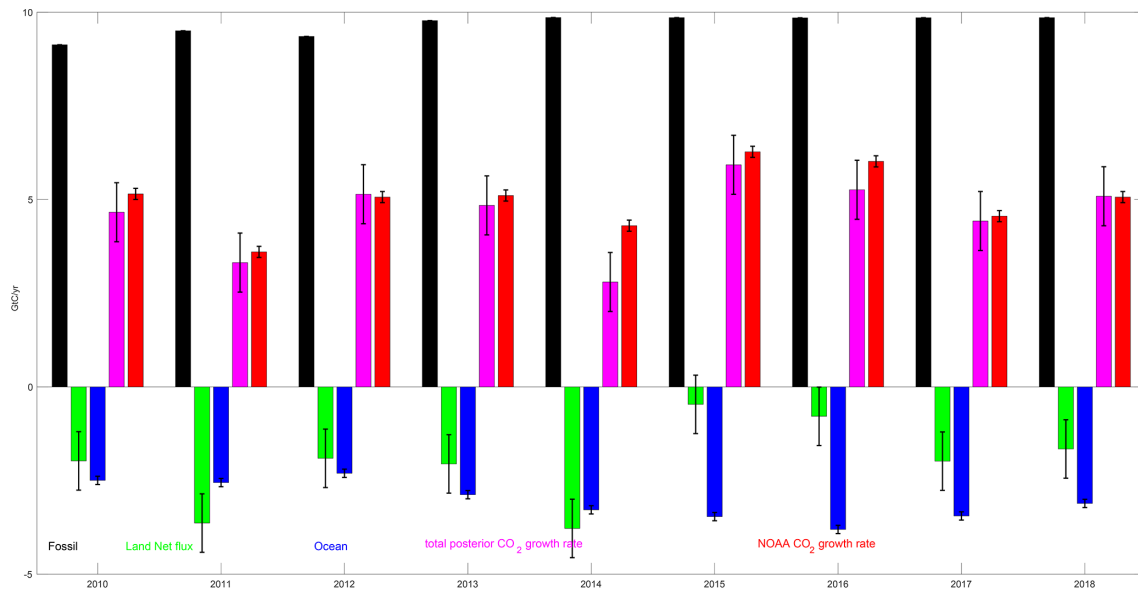
Figure 4. Global flux estimation and uncertainties from 2010–2018 (black: fossil fuel; green: posterior land fluxes; blue: ocean fluxes; magenta: estimated CO_2 growth rate; red: the NOAA CO_2 growth rate).

reported by Freidlingstein et al. (2019), where S_{LAND} is terrestrial sink, B_{IM} is a budget imbalance, and E_{LUC} is land use change. Over these 9 years, we estimate that NBE ranges from 3.6 Gt C ($\sim 37\%$ of fossil fuel emissions) in 2011 (a La Niña year) to only 0.5 Gt C ($\sim 5\%$ of fossil fuel emissions) in 2015 (an El Niño year), consistent with 3.3 Gt C (35 % of fossil fuel) in 2011 to 0.9 Gt C (7 % of fossil fuel) in 2015 estimated from GCB-2019. We estimate that the ocean sinks range from 3.5 Gt C in 2015 to 2.3 Gt C in 2012, which is larger than the estimated ocean flux ranges of 2.7 in 2016 to 2.5 in 2012 reported by Freidlingstein et al. (2019).

4.2 Mean regional fluxes and uncertainties

Figure 5 shows the 9-year mean regional annual fluxes, uncertainty, and its variability between 2010–2018. Table 6 shows an example of the dataset corresponding to Fig. 5a, d, and g. It shows that large net carbon uptake occurs over Eurasia, NA, and the Southern Hemisphere (SH) midlatitudes. The largest net carbon uptake is over the eastern US (-0.4 ± 0.1 Gt C (1σ uncertainty)) and high-latitude Eurasia (-0.5 ± 0.1 Gt C) (Fig. 5a, b). We estimate a net land carbon sink of 2.5 ± 0.3 Gt C/yr between 2010–2013 over the NH mid- to high latitudes, which agrees with 2.4 ± 0.6 Gt C estimates over the same time periods based on a two-box model (Ciais et al., 2019). Net uptake in the tropics ranges from close to neutral in tropical South America (0.1 ± 0.1 Gt C) to a net source in northern Africa (0.6 ± 0.2 Gt C) (Fig. 5a, b). The tropics exhibit both large uncertainty and large variability. The NBE interannual variabilities over northern Africa and tropical SA are 0.5 and 0.3 Gt C, respectively, which are larger than the 0.2 and 0.1 Gt C uncertainty (Fig. 5d,

e). We also find collocation of regions with large NBE and FLUXSAT GPP interannual variability (Fig. B4). The availability of flux estimates over the broadly used TransCom regions makes it easy to compare to previous studies. For example, we estimate that the annual net carbon uptake over North America is 0.7 ± 0.1 Gt C/yr with 0.2 Gt C variability between 2010 and 2018, which agrees with 0.7 ± 0.5 Gt C/yr estimates based on surface CO_2 observations between 1996–2007 (Peylin et al., 2013).

4.3 Interannual variabilities and uncertainties

Here we present hemispheric and regional NBE interannual variabilities and corresponding uncertainties (Figs. 6 and 7, and corresponding tabular data files). In Fig. 6, we further divide the globe into three large latitude bands: tropics (20° S–20° N), NH extra-tropics (20–85° N), and SH extra-tropics (60–20° S). The tropical NBE contributes 90 % to the global NBE interannual variability (IAV). The IAV of NBE over the extra-tropics is only about one-third of that over the tropics. The dominant role of tropical NBE in the global IAV of NBE agrees with Fig. 4 in Sellers et al. (2018). The top-down global annual NBE anomaly is within the 1.0 Gt C/yr uncertainty of residual NBE (i.e., fossil fuel–atmospheric growth–ocean sink) calculated from GCB-2019 (Friedlinston et al., 2019) (Fig. 6).

Figure 7 shows the annual NBE anomalies and uncertainties over a few selected regions based on RM1. Positive NBE indicates reduced net uptake relative to the 2010–2018 mean, and vice versa. Also shown in Fig. 7 are GPP anomalies estimated from FLUXSAT. Positive GPP indicates increased productivity, and vice versa. GPP drives NBE in years where
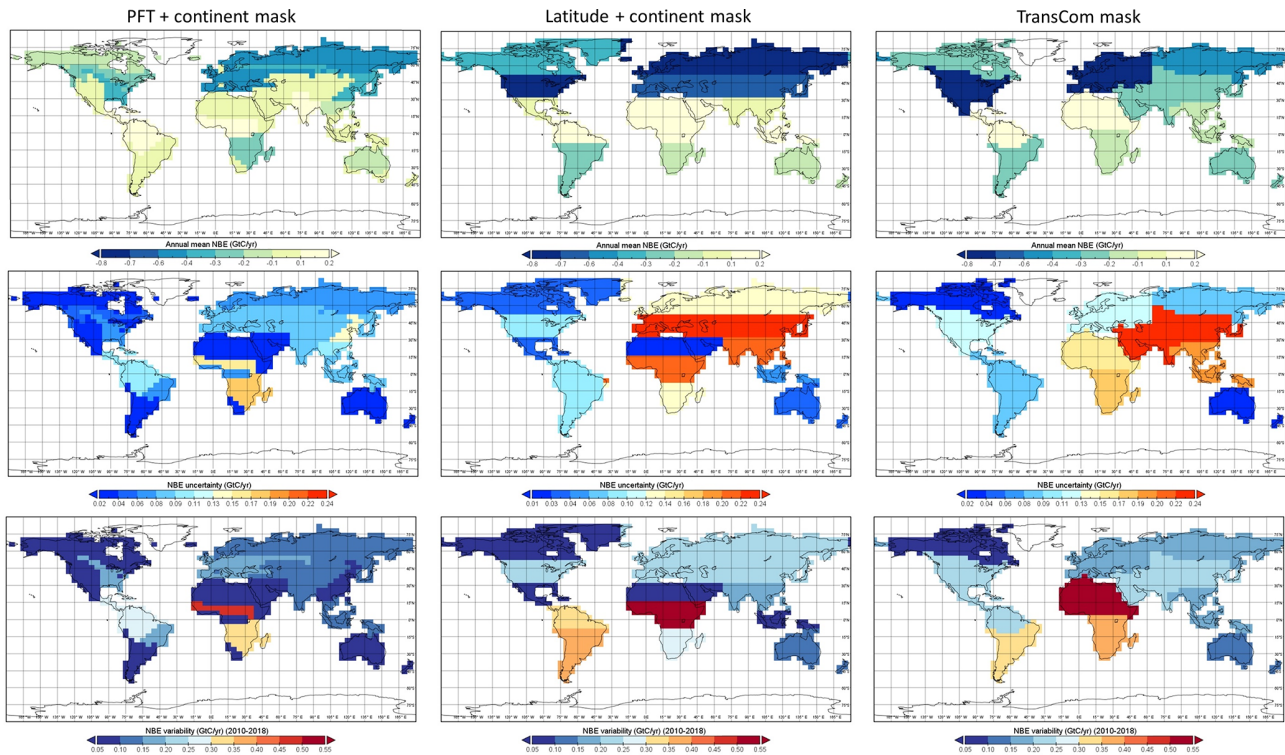
Figure 5. Mean annual regional NBE **(a, b, c)**, uncertainty **(d, e, f)**, and variability between 2010–2018 **(g, h, i)** with the three types of regional masks (Fig. 3). The first column uses a region mask based on plant functional types (PFTs) and continents (RM1). The second column uses a region mask based on latitude and continents (RM2), and the third column uses a TransCom mask.
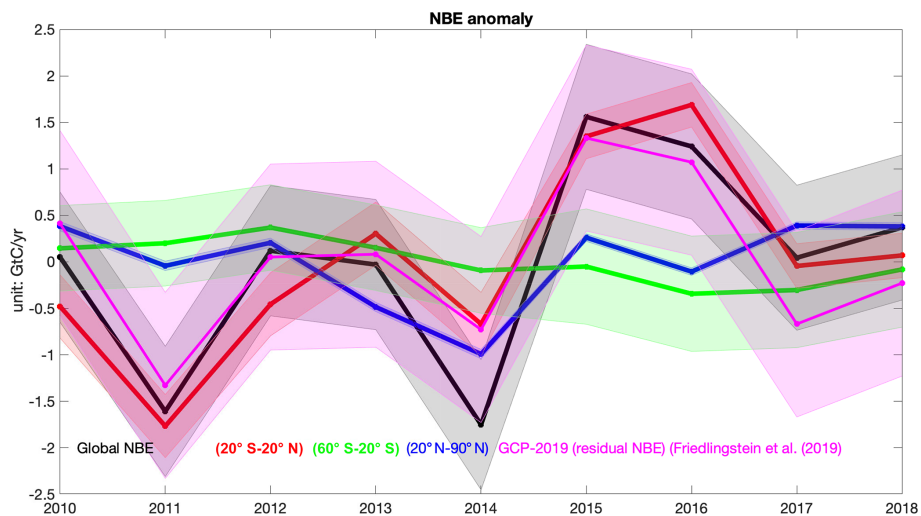

Figure 6. The NBE interannual variability over the globe (black), the tropics (20° S–20° N), SH midlatitudes (60–20° S), and NH midlatitudes (20–90° N). For reference, the residual net land carbon sink from GCB-2019 (Friedlingstein et al., 2019) and its uncertainty is also shown (magenta).

anomalies are inversely correlated (e.g., positive NBE and negative GPP), and TER drives NBE in years where anomalies of GPP and NBE have the same sign or are weakly correlated. Over tropical SA evergreen broadleaf forest, the largest positive NBE anomalies occur during the 2015–2016

El Niño, corresponding to large reductions in productivity, consistent with Liu et al. (2017). In 2017, the region sees increased net uptake and increased productivity, implying a recovery from the 2015–2016 El Niño event. The variability in GPP explains 80 % of NBE variability over this region
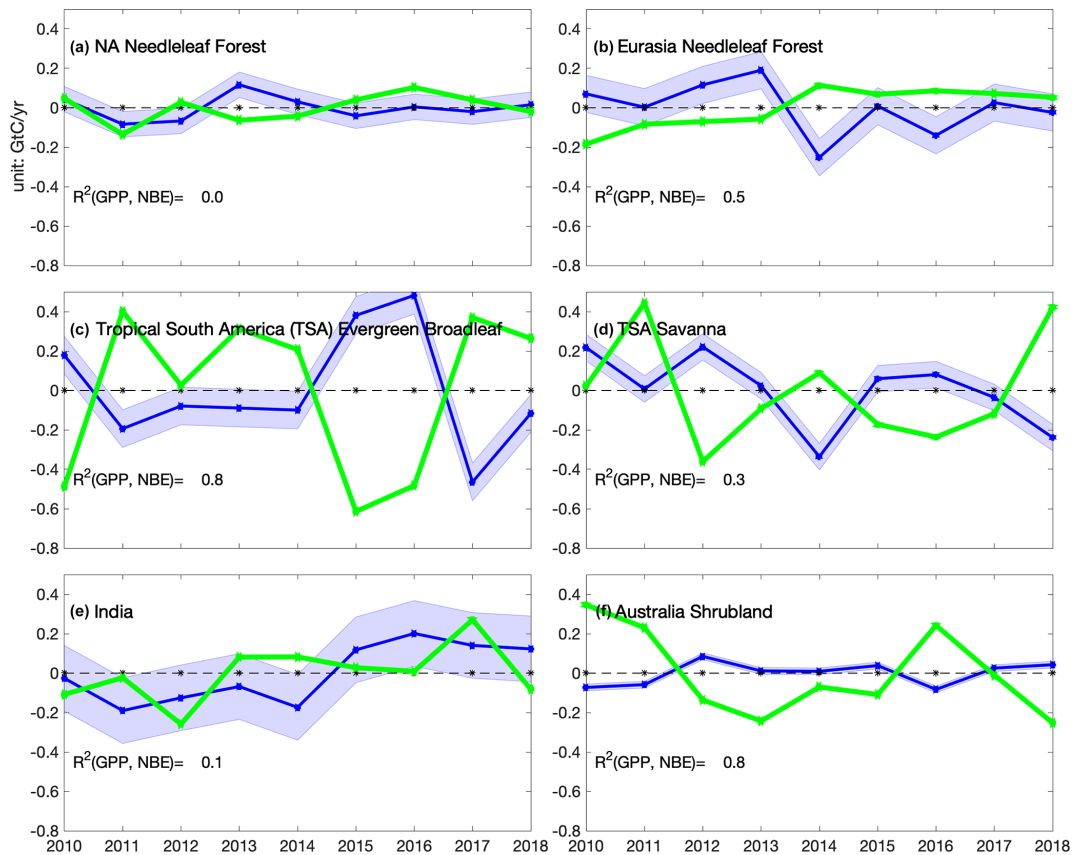
Figure 7. The NBE interannual variability over six selected regions. Blue: annual NBE anomaly and its uncertainties. Green: annual GPP anomaly based on FLUXSAT.

over the 9-year period. In Australian shrubland, our inversion captures the increased net uptake in 2010 and 2011 due to increased precipitation (Poulter et al., 2014) and increased productivity. The variability in GPP explains 70 % of the interannual variability in NBE. Over tropical South America savanna, the NBE interannual variability also shows strong negative correlations with GPP, with GPP explaining 40 % of NBE interannual variability. Over the midlatitude regions where the IAV is small, the R^2 between GPP and NBE is also small (0.0–0.5) as expected. But the increased net uptake generally corresponds to increased productivity. We also do not expect perfect negative correlation between NBE anomalies and GPP anomalies, as discussed in Sect. 2.5. The comparison between NBE and GPP provides insight into when and where net fluxes are likely dominated by productivity.

4.4   Seasonal cycle

We provide the regional mean NBE seasonal cycle, its variability, and uncertainty based on the three regional masks (Table 5). Here we briefly describe the characteristics of the NBE seasonal cycle over the 11 TransCom regions and its comparison to three independent top-down inversion results based on surface CO_2, which are CT-Europe (e.g., van der

Laan-Luijkx et al., 2017), CAMS (Chevallier et al., 2005), and Jena CarbonScope (Rödenbeck et al., 2003). CMS-Flux NBE differs the most from surface-CO_2-based inversions over the South American tropical, northern Africa, tropical Asia, and NH boreal regions. The CMS-Flux NBE has a larger seasonal cycle amplitude over tropical Asia and northern Africa, where the surface CO_2 constraint is weak, while it has a smaller seasonal cycle amplitude over the boreal region; this may be due to the sparse satellite observations over the high latitudes and weaker seasonal amplitude of the prior CARDAMOM fluxes. The comparison to FLUXSAT GPP can only qualitatively evaluate the NBE seasonal cycle but cannot differentiate among different estimates. In general, the months that have larger productivity correspond to months with a net uptake of carbon from the atmosphere, especially over the NH (Fig. 8). More research is still needed to understand the seasonal cycles of NBE, including its phase (i.e., transition from source to sink) and amplitude (peak-to-trough difference), as well as its relationships with GPP and respiration.

Table 5. List of the data products.

Product	Spatial resolution	Temporal resolution when applicable	Data format	Sample data description in the text
Total fossil fuel, ocean, and land fluxes	Global	Annual	csv	Fig. 4 (Sect. 4.1)
Climatology mean NBE, variability, and uncertainties	PFT- and continent-based 28 regions	n/a	csv	Fig. 5 (Sect. 4.2)
	Geographic-based 13 regions		csv	
	TransCom regions		csv	
Hemispheric NBE and uncertainties	NH (20–90° N), tropics (20° S–20° N), and SH (60–20° S)	Annual	csv	Fig. 6 (Sect. 4.3)
NBE variability and uncertainties	PFT- and continent-based 28 regions	Annual	csv	Fig. 7 (Sect. 4.3)
	Geographic-based 13 regions		csv	
	TransCom regions		csv	
NBE seasonality and its uncertainties	PFT- and continent-based 28 regions	Monthly	csv	Fig. 8 (Sect. 4.4)
	Geographic-based 13 regions		csv	
	TransCom regions		csv	
Monthly NBE and uncertainties	PFT- and continent-based 28 regions	Monthly	csv	n/a
	Geographic-based 13 regions		csv	
	TransCom		csv	
Gridded posterior NBE, air–sea carbon exchanges, and uncertainties	4° (latitude) × 5° (longitude)	Monthly	NetCDF	n/a
Gridded prior NBE and air–sea carbon exchanges	4° (latitude) × 5° (longitude)	Monthly and 3-hourly	NetCDF	n/a
Gridded fossil fuel emissions	4° (latitude) × 5° (longitude)	Monthly mean and hourly	NetCDF	n/a
Region masks	PFT- and continent-based 28 regions	n/a	csv	Fig. 3 (Sect. 2.4)
	Geographic-based 13 regions			
	TransCom regions			

n/a: not applicable.

5 Evaluation against independent aircraft CO_2 observations

5.1 Comparison to aircraft observations over nine sub-regions

In this section, we evaluate posterior CO_2 against aircraft observations over the nine sub-regions listed in Table 4 and Fig. 2. We compare the posterior CO_2 to aircraft CO_2 mole fractions above the planetary boundary layer and up to the mid-troposphere (1–5 km) at the locations and time of aircraft observations, and then we calculate the monthly mean error statistics between 1–5 km. The aircraft observations between 1–5 km are more sensitive to regional fluxes (Liu et al., 2015; Liu and Bowman, 2016). Scatter plots in the left col-

umn of Fig. 9 show regional monthly mean detrended aircraft CO_2 observations (x axis) versus the simulated detrended posterior CO_2 (y axis). We used the NOAA global CO_2 trend to detrend both the observations and model-simulated mole fractions (ftp://aftp.cmdl.noaa.gov/products/trends/co2/co2_trend_gl.txt, last access: 19 May 2020). Over the NH regions (Fig. 9a, b, c, d) and Africa (Fig. 9f), the R^2 is greater than or equal to 0.9, which indicates that the posterior CO_2 captures the observed seasonality. The low R^2 (0.7) value in South Asia is caused by one outlier. Over the Southern Ocean, Australia, and SA, the R^2 is between 0.2 and 0.4, reflecting weaker CO_2 seasonality over these regions and possible bias in ocean flux estimates (see discussions later).

The right panel of Fig. 9 shows the monthly mean differences between posterior CO_2 and aircraft observations

Table 6. The 9-year mean regional annual fluxes, uncertainties, and variability. Regions are based on the mask shown in Fig. 5a (Figure5.csv). Unit: Gt C/yr.

Region name (Figure4.csv)	Mean NBE	Uncertainty	Variability
NA shrubland	−0.14	0.02	0.05
NA needleleaf forest	−0.22	0.04	0.06
NA deciduous forest	−0.2	0.04	0.07
NA crop natural vegetation	−0.41	0.06	0.18
NA grassland	−0.04	0.03	0.03
NA savanna	0.03	0.02	0.03
Tropical South America (SA) evergreen broadleaf	0.04	0.1	0.28
SA savanna	−0.09	0.06	0.18
SA cropland	−0.07	0.03	0.07
SA shrubland	−0.03	0.02	0.08
Eurasia shrubland savanna	−0.44	0.07	0.14
Eurasia needleleaf forest	−0.41	0.07	0.12
Europe cropland	−0.46	0.09	0.16
Eurasia grassland	0.02	0.08	0.13
Asia cropland	−0.37	0.13	0.08
India	0.14	0.09	0.14
Tropical Asia savanna	−0.12	0.11	0.08
Tropical Asia evergreen broadleaf	−0.09	0.09	0.12
Australian savanna grassland	−0.11	0.02	0.09
Australian shrubland	−0.07	0.01	0.05
Australian cropland	−0.01	0.01	0.03
African northern shrubland	0.04	0.02	0.03
African grassland	0.03	0.01	0.01
African northern savanna	0.54	0.15	0.49
African southern savanna	−0.27	0.18	0.33
African evergreen broadleaf	0.1	0.07	0.09
African southern shrubland	0.01	0.01	0.01
African desert	0.06	0.01	0.04

(black), RMSE (Eq. 2) (blue line), and $RMSE_{MC}$ (Eq. 3) (red line). The magnitude of the mean differences between the posterior CO_2 and aircraft observations is less than 0.5 ppm, except over the Southern Ocean, which has a −0.8 ppm bias. The mean differences between posterior CO_2 and aircraft observations are primarily caused by errors in transport and biases in assimilated satellite observations, while $RMSE_{MC}$ is the internal flux error projected into mole fraction space. With the exception of the Southern Ocean, for all regions mean bias is significantly less than $RMSE_{MC}$, which suggests that transport and data bias in satellite observations may be much smaller than the internal flux errors. Note that $RMSE_{MC}$ is smaller than RMSE over the first ~ 6 months of simulation, which may indicate a dominant impact of errors in transport and initial CO_2 concentration on posterior CO_2 RMSE.

As demonstrated in Sect. 2.5, comparing RMSE and $RMSE_{MC}$ is a test of the accuracy of posterior flux uncertainty estimate. Over all the regions, the differences between RMSE and $RMSE_{MC}$ are smaller than 0.3 ppm, which indicates a comparable magnitude between empirical posterior flux uncertainty estimates from the Monte Carlo method

and the actual posterior flux uncertainty over the regions that these aircraft observations are sensitive to. These aircraft observations are sensitive to NBE over a broad region as shown in Fig. B5. Note that Figs. B5 and B8–B10 are calculated using Eq. (8).

5.2 Comparison to aircraft observations from ATom and HIPPO aircraft campaigns

Figures 10 and 11 show comparisons to aircraft CO_2 from the ATom 1–4 campaigns spanning four seasons and HIPPO 3–5 over the Pacific Ocean between 1–5 km. The vertical curtain comparisons are shown in Figs. B6 and B7. The mean differences between posterior CO_2 and aircraft CO_2 are quite uniform (within 0.5 ppm) throughout the column, except over the Atlantic Ocean during ATom 1–2 and the Southern Ocean during ATom 1 (Figs. S6 and S7). Also shown in Figs. 10 and 11 are RMSEs of each aircraft campaign (middle column) and the ratio between RMSE and $RMSE_{MC}$ (right column). A ratio larger than one between RMSE and $RMSE_{MC}$ indicates errors in either transport or underestimation of the posterior flux uncertainty (Sect. 2.5).
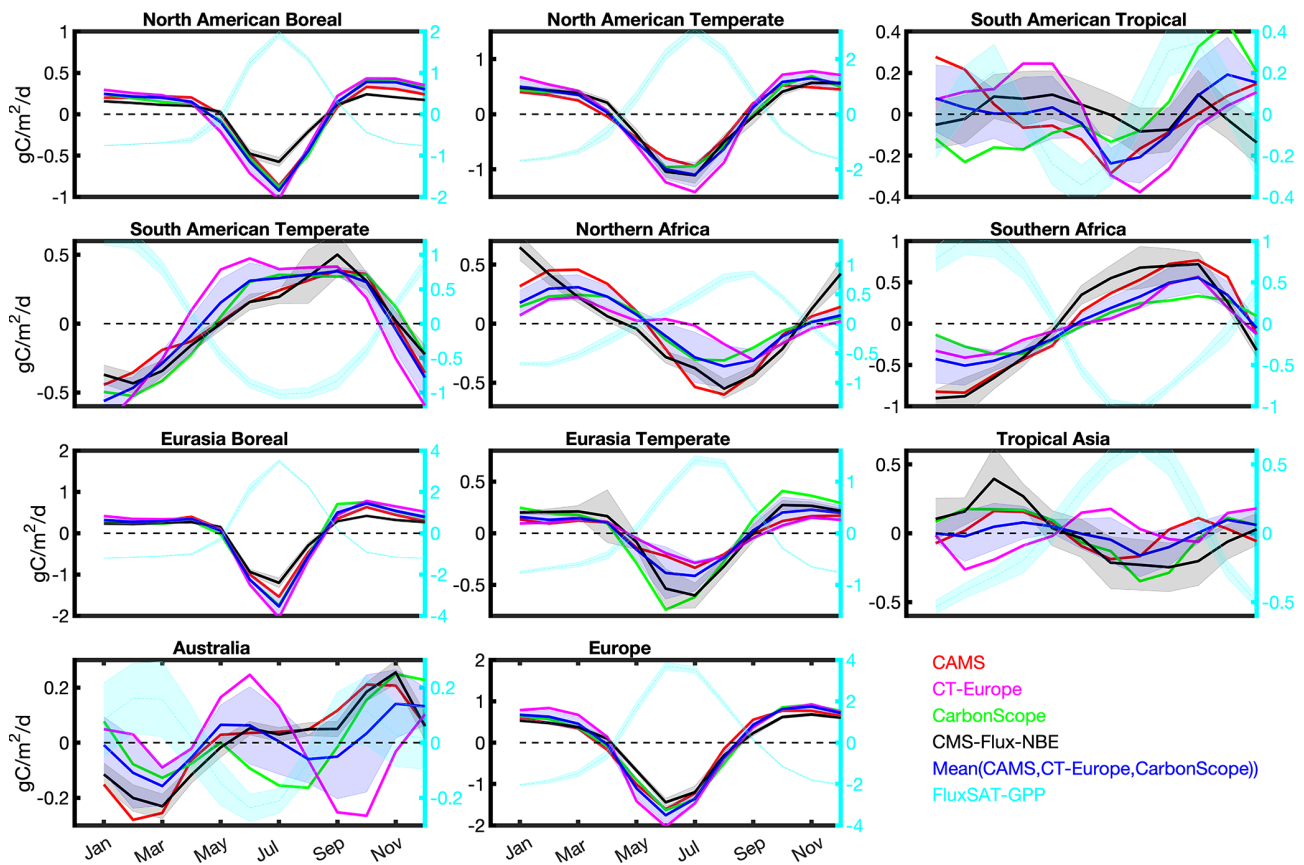
Figure 8. The NBE climatological seasonality over TransCom regions. The seasonal cycle is calculated over 2010–2017 since CT-Europe only covers until 2017. Black: CMS-Flux NBE and its uncertainty; blue shaded: mean NBE seasonality based on surface CO_2 inversion results from CAMS, CT-Europe, and Jena CarbonScope; red: CAMS; magenta: CT-Europe; green: Jena CarbonScope. The names of each region are shown on individual subplots.

Over most of the flight tracks during ATom 1–4, the posterior CO_2 errors are between −0.5 and 0.5 ppm, the RMSE is smaller than 0.5 ppm, and the ratio between RMSE and $RMSE_{MC}$ is smaller than or equal to 1. However, off the coast of Africa during ATom 1 and 2 and over the Southern Ocean during ATom 1, the mean differences between posterior CO_2 and aircraft observations are larger than 0.5 ppm. During ATom 1 (29 July–23 August 2016), the mean differences between posterior CO_2 and aircraft CO_2 show large negative biases, while during ATom 2 (26 January–21 February 2017) it has large positive biases off the coast of Africa. The ratio between RMSE and $RMSE_{MC}$ is significantly larger than one over these regions, which indicates an underestimation of posterior flux uncertainty or a large magnitude of transport errors during that time period.

We further run adjoint sensitivity analyses over the three regions with ratios significantly larger than one to identify the posterior fluxes that could contribute to the large differences between posterior CO_2 and aircraft observations during ATom 1–2. We run the adjoint model backward for 3 months from the observation time and calculate S_i as defined in Eq. (7). The adjoint sensitivity analysis indicates that the large mismatch between aircraft observations and model simulations during ATom 1 and -2 off the coast of Africa could be potentially driven by errors in posterior fluxes over tropical Africa (Fig. B8). The large posterior CO_2 errors and large ratio between RMSE and $RMSE_{MC}$ over the Southern Ocean during ATom 1 are driven by flux errors in oceanic fluxes around 30° S and over Australia (Fig. B9), which also contribute to the large errors in comparison to aircraft observations over the Southern Ocean shown in Fig. 9h.

During the HIPPO aircraft campaigns, the absolute errors in posterior CO_2 across the Pacific are less than 0.5 ppm, except over the Arctic Ocean and over Alaska in summer (Fig. 11), consistent with Fig. 10a. The large errors over the Arctic Ocean may be related to both transport errors and the accuracy of high-latitude fluxes. Byrne et al. (2020) provide a brief summary of the challenges in simulating CO_2 over high latitudes using a transport model with 4° × 5° resolution. Increasing the resolution of the transport model may reduce transport errors over high latitudes.
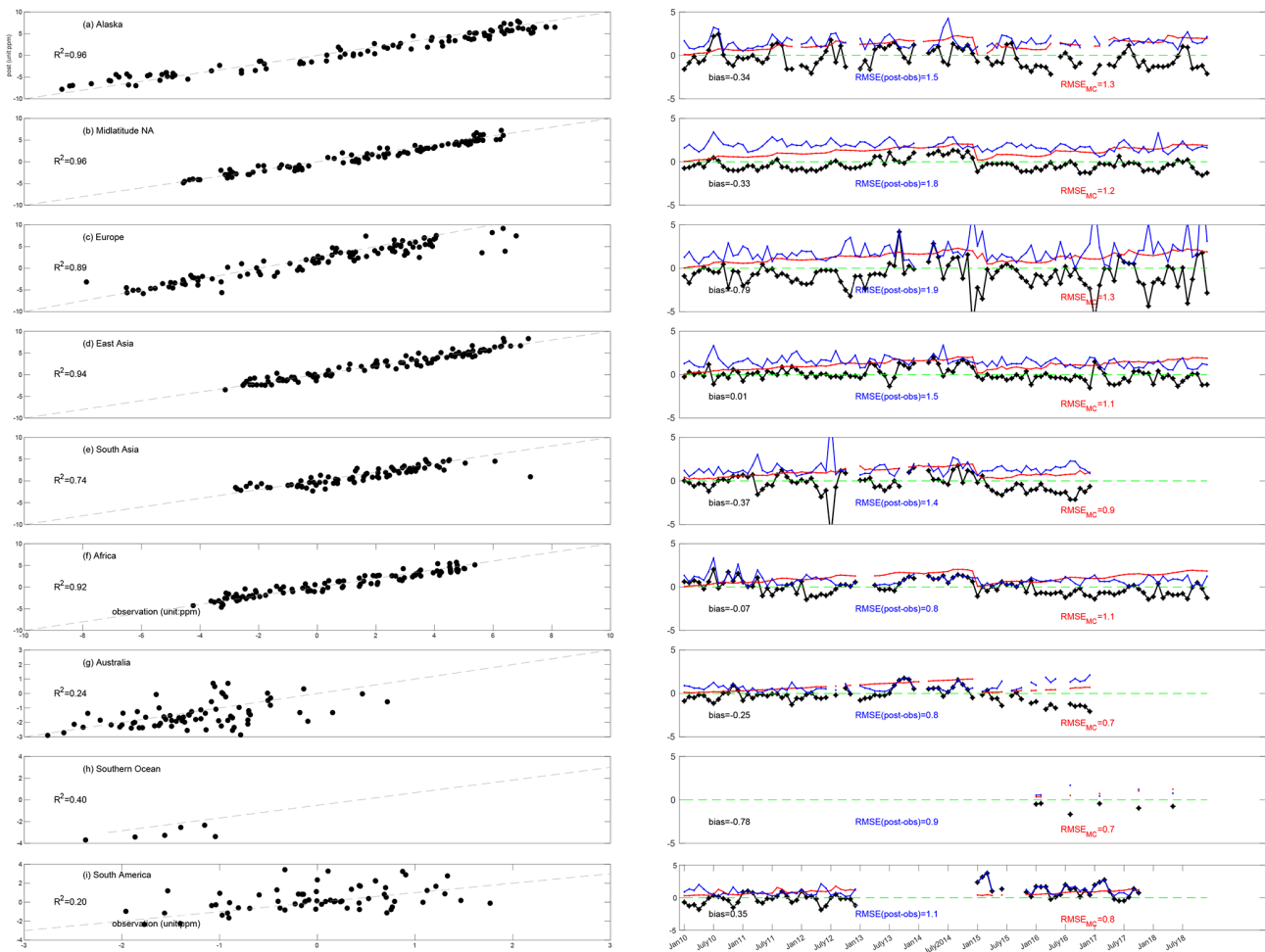
Figure 9. Comparison between posterior CO_2 mole fraction and aircraft observations. Left panel: detrended posterior CO_2 (y axis) vs. detrended aircraft CO_2 (x axis) over nine regions. The dashed line is the one-to-one line; right panel: the differences between posterior CO_2 and aircraft CO_2 as a function of time (black), RMSE (blue; unit: ppm), and $RMSE_{MC}$ (red).

We run adjoint sensitivity analyses over the high-latitude regions where the differences between posterior CO_2 and aircraft observations are large (Fig. 11). The adjoint sensitivity analysis (Fig. B10) shows that the large errors over these regions could be driven by errors in fluxes over Alaska as well as broad NH midlatitude regions.

5.3 Comparison to MBL reference sites

Since MBL reference sites sample air over broad regions, the comparison to detrended MBL observations indirectly evaluates the NBE over large regions. Figure 12 shows the comparison over four latitude bands. The uncertainty of posterior CO_2 concentration is from the MC method. Except over 90–20° S, the differences between observations and posterior CO_2 are within posterior CO_2 uncertainty estimates. The posterior CO_2 concentrations have the smallest bias and random errors over the tropical latitude band. The R^2 is above 0.9 over NH mid- to high latitudes, consistent with Fig. 9.

Over 90–20° S, the posterior CO_2 has positive bias in 2013 and 2014 and negative bias and much weaker seasonality between January 2015–December 2018 compared to observations, which indicates possible biases in Southern Ocean flux estimates (Fig. B11). The low bias over the Southern Ocean is consistent with aircraft comparison during the OCO-2 period (Figs. 9–10, B9). The changes of performance after 2013 over 90–20° S are most likely due to the prior ocean carbon fluxes. Evaluation of ocean carbon fluxes is out of the scope of this study. Note that since we only assimilate land nadir X_{CO_2} observations in this study due to known issues with the OCO-2 v9 ocean glint observations (O'Dell et all., 2018), the constraint of top-down inversion on air–sea CO_2 exchanges is weak (not shown). The ocean glint observations of OCO-2 v10 observations have been improved compared to v9 (Osterman et al., 2020). We expect to have a better estimate of ocean carbon fluxes over the Southern Ocean when assimilating both land and ocean X_{CO_2} observations from GOSAT and OCO-2 in the future.

Earth Syst. Sci. Data, 13, 299–330, 2021

https://doi.org/10.5194/essd-13-299-2021
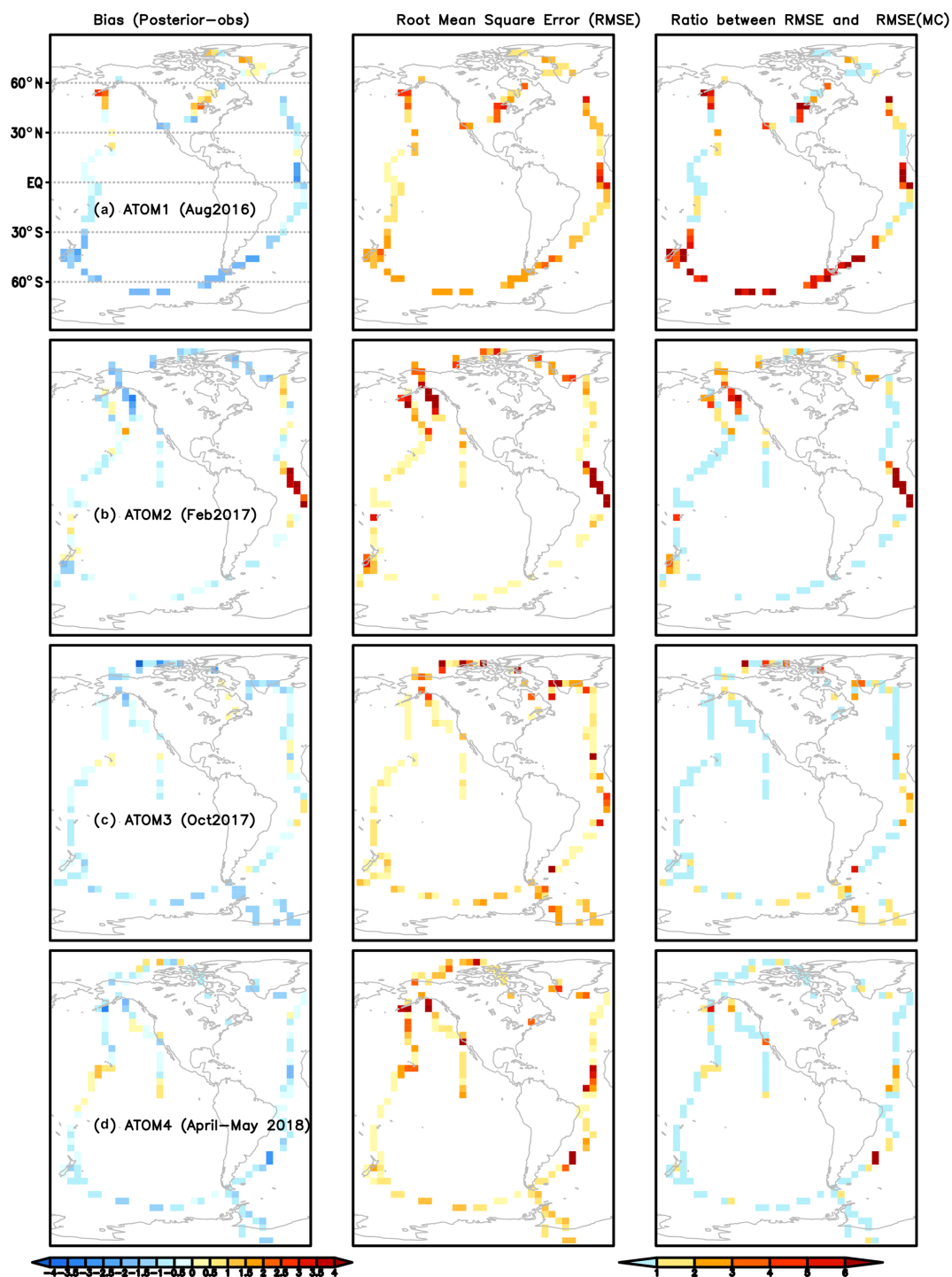
Figure 10. Left column: the mean differences between posterior CO_2 and aircraft observations from ATom 1–4 aircraft campaigns between 1–5 km (**a–d**). Middle column: the root mean square errors (RMSEs) between aircraft observations and posterior CO_2 between 1–5 km. The color bar is the same as in the left column. Right column: the ratio between RMSE and $RMSE_{MC}$ based on ensemble CO_2 from the Monte Carlo uncertainty estimation method.
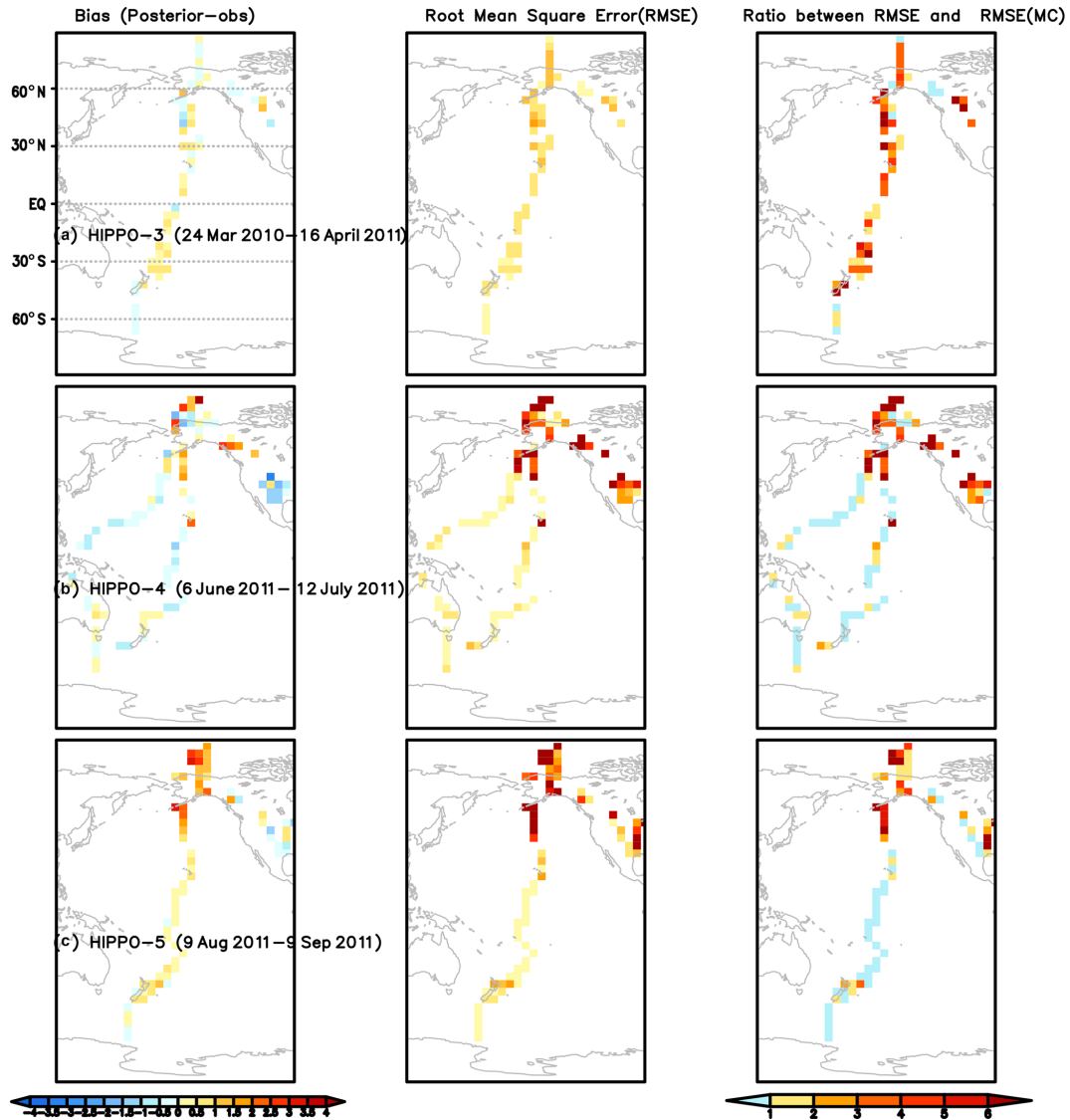
Figure 11. Left column: the mean differences between posterior CO_2 and aircraft observations from HIPPO 3–5 aircraft campaigns between 1–5 km **(a–c)** (unit: ppm). The time frame of each campaign is in the figure. Middle column: the root mean square errors (RMSEs) between aircraft observations and posterior CO_2 between 1–5 km (unit: ppm). The color bar is the same as in the left column. Right column: the ratio between RMSE and $RMSE_{MC}$ based on ensemble CO_2 from the Monte Carlo method.

6   Discussion

Evaluation of posterior flux uncertainty estimates by comparing posterior CO_2 error statistics (RMSE, Eq. 2) with the standard deviation of ensemble simulated CO_2 from the Monte Carlo uncertainty quantification method ($RMSE_{MC}$, Eq. 3) has its limitations. A comparable RMSE and $RMSE_{MC}$ indicates a small magnitude of transport errors and reasonable posterior uncertainty estimates. A much larger RMSE than $RMSE_{MC}$ could be due to errors in either transport or underestimation of the posterior flux uncertainty or both. The presence of transport errors makes the interpretation of the RMSE and $RMSE_{MC}$ complex. A better, independent quantification of transport errors is needed in the future in order to rigorously use the comparison statistics between aircraft observations and posterior CO_2 to diagnose flux errors.

Comparison to aircraft observations shows regionally dependent accuracy in posterior fluxes. ATom observations show seasonally dependent biases over the Atlantic, implying possible seasonally dependent errors in posterior fluxes over northern to central Africa. Therefore, we recommend combining NBE with other ancillary variables, e.g., GPP, to better understand carbon dynamics. Combining NBE with component carbon fluxes can shed light on the processes controlling the changes of NBE (e.g., Bowman et al., 2017; Liu
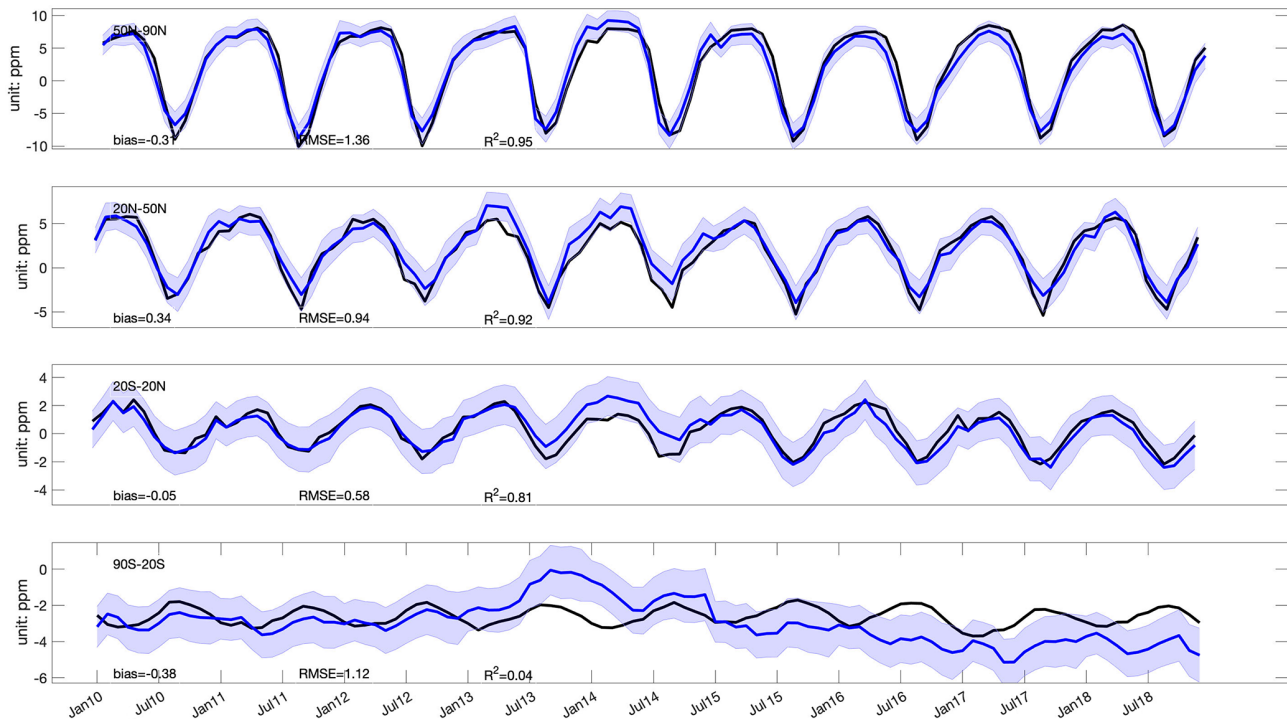
Figure 12. Comparison between posterior CO_2 and the NOAA marine boundary layer (MBL) reference sites. Black: observations averaged over each latitude band; blue and shaded area: posterior CO_2 and its uncertainty. The global mean CO_2 (https://www.esrl.noaa.gov/gmd/ccgg/trends/global.html, last access: 29 May 2020) was subtracted from both the NOAA MBL reference and posterior CO_2 before the comparison.

et al., 2017). NBE can be written as

$$NBE = TER + fire − GPP, \tag{9}$$

where TER is total ecosystem respiration (TER) (Fig. 1). Satellite carbon monoxide (CO) observations provide constraints on fire emissions (Arellano et al., 2006; van der Werf, 2008; Jones et al., 2009; Jiang et al., 2017; Bowman et al., 2017; Liu et al., 2017). In addition to the FLUXSAT GPP product used here, solar-induced chlorophyll fluorescence (SIF) can be directly used as a proxy for GPP (e.g., Parazoo et al., 2014). Once NBE, fire, and GPP carbon fluxes are quantified, TER can be calculated as a residual (e.g., Bowman et al., 2017; Liu et al., 2017, 2018).

Because of the diffusive manner of atmospheric transport and the limited observation coverage, the gridded flux values are not independent from each other. The errors and uncertainties of the fluxes at each individual grid point are larger than regional aggregated fluxes. Interpreting NBE at each individual grid point requires caution. But at the same time, satellite CO_2-constrained NBE can potentially resolve fluxes at spatial scales smaller than the traditional TransCom regions. Here, we provide regional fluxes at two predefined regions in addition to TransCom. We encourage data users to use the data at appropriate regional scales.

The variability and changes are more robust than the mean NBE fluxes from top-down flux inversions in general (Baker et al., 2006b). The errors in transport and potential biases in

observations are mostly stable in time, so biases in the mean fluxes tend to cancel out when computing interannual variability and year-to-year changes (Schuh et al., 2019; Crowell et al., 2019).

The global fossil fuel emissions have $\sim 5\%$ uncertainty (GCB-2019). However, they are regionally inhomogeneous. We neglect the uncertainties in fossil fuel emissions, which will introduce additional error in regions of rapid fossil fuel growth or in areas with noisier statistics (Yin et al., 2019). In the future, we will account for uncertainties in fossil fuel emissions.

The posterior NBE includes all types of land fluxes except fossil fuel emissions, which is equivalent to the sum of land use change fluxes, land sinks, and residual imbalance published by the GCB-2019. The sum of regional NBE and fossil fuel emissions is an index of the contribution of any specific region to the changes of the atmospheric CO_2 growth rate. Since the predicted changes of NBE in the future have large uncertainties (Lovenduski and Bonan, 2017), quantifying regional NBE is critical to monitoring regional contributions to atmospheric CO_2 growth rate and ultimately to guiding mitigation to limit warming to $1.5\,°C$ above pre-industrial levels (IPCC, 2021).

Table 7. Lists of data sources used in producing and evaluating the posterior NBE product.

Data name	Data source
ECCO-Darwin ocean fluxes	https://doi.org/10.25966/4v02-c391 (last access: 10 June 2020)
CARDAMOM NBE and uncertainties	https://doi.org/10.25966/4v02-c391 (last access: 10 June 2020)
ODIAC	http://db.cger.nies.go.jp/dataset/ODIAC/DL_odiac2019.html (last access: 15 September 2019)
GOSAT b7.3	https://oco2.gesdisc.eosdis.nasa.gov/data/GOSAT_TANSO_Level2/ACOS_L2S.7.3/ (last access: 4 October 2019)
OCO-2 b9	https://disc.gsfc.nasa.gov/datasets?page=1&keywords=OCO-2 (last access: 4 October 2019)
ObsPack	https://www.esrl.noaa.gov/gmd/ccgg/obspack/data.php (last access: 4 October 2019)
ATom 1–4	https://daac.ornl.gov/ATOM/guides/ATom_merge.html (last access: 10 March 2020)
HIPPO 3–5	https://www.eol.ucar.edu/field_projects/hippo (last access: 10 March 2020)
INPE	https://www.esrl.noaa.gov/gmd/ccgg/obspack/data.php?id=_obspack_co2_1_INPE_RESTRICTED_v2.0_2018-11-13 (last access: 10 March 2020) and
FLUXSAT GPP	https://gs614-avdc1-pz.gsfc.nasa.gov/pub/tmp/FluxSat_GPP/ (last access: 10 March 2020)
NOAA MBL reference	https://www.esrl.noaa.gov/gmd/ccgg/mbl/index.html (last access: 1 September 2020)
CarbonTracker Europe NBE	https://www.carbontracker.eu/download.shtml (last access: 1 September 2020)
Jena CarbonScope NBE	http://www.bgc-jena.mpg.de/CarboScope/?ID=s (last access: 1 September 2020)
CAMS NBE	https://apps.ecmwf.int/datasets/data/cams-ghg-inversions/?date_month_slider=2009-12,2018-12&param=co2&datatype=ra&version=v17r1&frequency=mm&quantity=surface_flux (last access: 1 September 2020)
Posterior NBE	https://doi.org/10.25966/4v02-c391 (last access: 10 June 2020)

7   Data availability

The CMS-Flux NBE 2020 data are available at https://doi.org/10.25966/4v02-c391 (Liu et al., 2020). The regional aggregated fluxes are provided as csv files with file size ~ 10 MB, and the gridded data are provided in NetCDF format with file size ~ 1.4 GB. The full ensemble of posterior fluxes used to estimate posterior flux uncertainties is provided in NetCDF format with file size ~ 30 MB. Table 7 lists the sources of the data used in producing and evaluating the CMS-Flux NBE 2020 data product.

The quality of X_{CO_2} from satellite observations is continually improving. The OCO-2 v10 X_{CO_2} was released in June 2020 along with the full GOSAT record (June 2009–January 2020) processed by the same retrieval algorithm as OCO-2. Continuing to improve the quality of satellite observations and extending the NBE estimates beyond 2018 in the future will help us better understand interactions between the terrestrial biosphere carbon cycle and climate and provide support in monitoring the regional contributions to the changes of atmospheric CO_2. Thus, we plan a future update of the dataset on an annual basis, with a goal to support current scientific research and policy making.

8   Summary

Terrestrial biosphere carbon fluxes are the largest contributor to the interannual variability of the atmospheric CO_2 growth rate. Therefore, monitoring its change at regional scales is essential for understanding how it responds to CO_2, climate, and land use. Here, we present the longest terrestrial

flux estimates and their uncertainties constrained by X_{CO_2} from 2010–2018 on self-consistent global and regional scales (CMS-Flux NBE 2020). We qualitatively evaluate the NBE estimates by comparing its variability with GPP variability and provide a comprehensive evaluation of posterior fluxes and the uncertainties by comparing posterior CO_2 with independent CO_2 observations from aircraft and the NOAA MBL reference sites. This dataset can be used in understanding controls on regional NBE interannual variability, evaluating biogeochemical models, and supporting the monitoring of regional contributions to changes in atmospheric CO_2.

Appendix A

As shown in Kalnay (2003),

$$\mathrm{RMSE}^2 = \frac{1}{n} \sum_{i=1}^{n} (\mathbf{R}_{i,i} + (\mathbf{HP}^a\mathbf{H}^T)_{i,i}), \tag{A1}$$

where $\mathbf{R}_{i,i}$ is the ith aircraft observation error variance, and $\mathbf{P}^a$ is the posterior flux error covariance. The $\mathbf{H}$ is the linearized observation operator, which transfers posterior flux errors to aircraft observation space, and $\mathbf{H}^T$ is its adjoint. In the Monte Carlo method, the posterior flux error covariance $\mathbf{P}^a$ is approximated by

$$\mathbf{P}^a = \frac{1}{n\mathrm{ens}}\mathbf{X}^a\mathbf{X}^{aT}, \tag{A2}$$

where $\mathbf{X}^a$ is the ensemble perturbations written as

$$\mathbf{X}^a = \mathbf{x}^a - \bar{\mathbf{x}}^a, \tag{A3}$$

where $\mathbf{x}^a$ is the ensemble posterior fluxes from the Monte Carlo simulations, and $\bar{\mathbf{x}}^a$ is the mean.

Therefore, $\mathbf{HP}^a\mathbf{H}^T$ can be written as

$$\mathbf{HP}^a\mathbf{H}^T = \frac{1}{n\mathrm{ens}}[h(\mathbf{x}^a) - h(\bar{\mathbf{x}}^a)][h(\mathbf{x}^a) - h(\bar{\mathbf{x}}^a)]^T. \tag{A4}$$

The sum of diagonal elements in the right-hand side of Eq. (A4) is the same as the definition of $\mathrm{RMSE}_{\mathrm{MC}}$ in the main text.

Therefore, when the posterior flux uncertainty estimated by the Monte Carlo method represents the actual uncertainty in posterior fluxes, Eq. (A1) can be written as

$$\mathrm{RMSE}^2 = \frac{1}{n} \sum_{i=1}^{n} \mathbf{R}_{i,i} + \mathrm{RMSE}_{\mathrm{MC}}^2. \tag{A5}$$

It is the same as Eq. (4) in the main text.

Appendix B

In this Appendix, we include figures to support the main text.
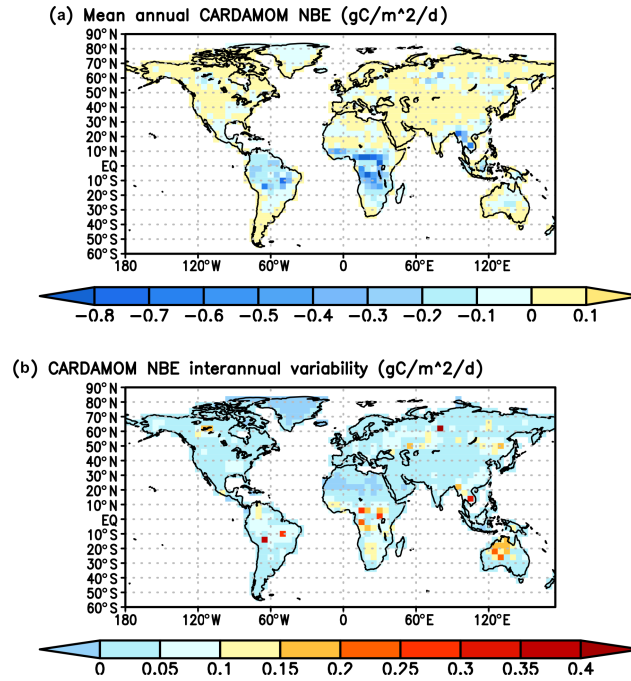
Figure B1. Annual mean net biosphere exchanges from CARDAMOM (**a**) and its interannual variability between 2010 and 2017 (**b**).
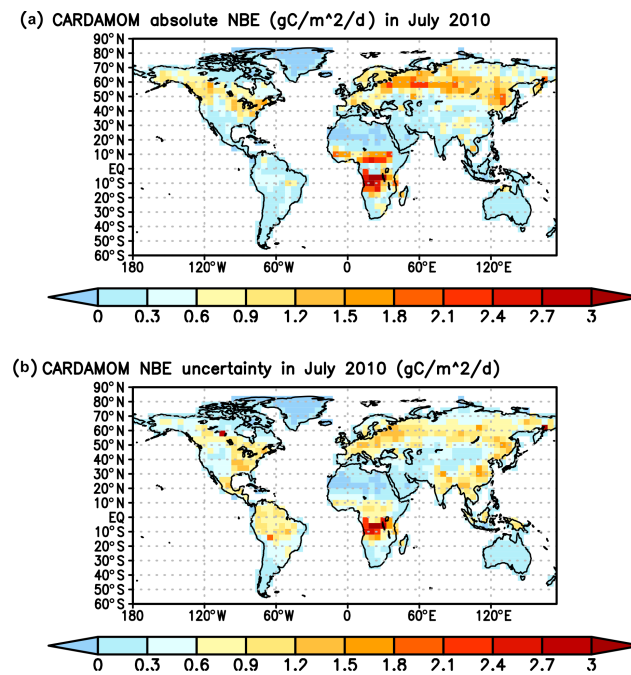
Figure B2. An example of absolute mean NBE (**a**) and its uncertainty (**b**) simulated by CARDAMOM. This is for July 2010.

Earth Syst. Sci. Data, 13, 299–330, 2021

https://doi.org/10.5194/essd-13-299-2021
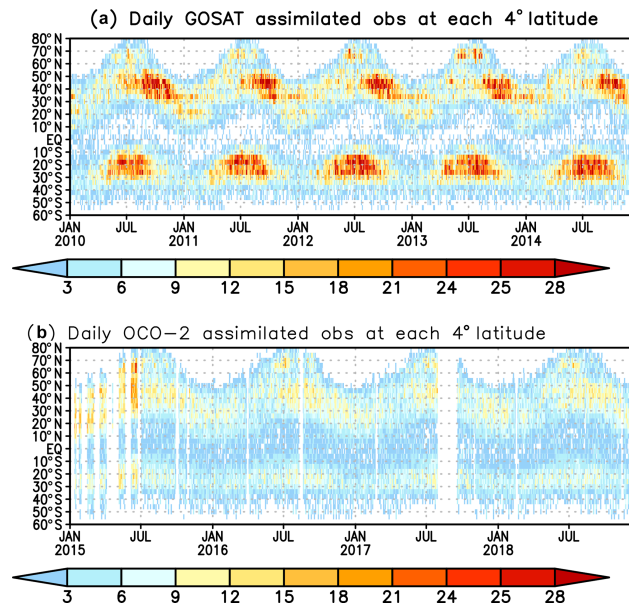
Figure B3. Daily number of ACOS-GOSAT b7.3 **(a)** and OCO-2 super observations **(b)** assimilated in the top-down inversions.
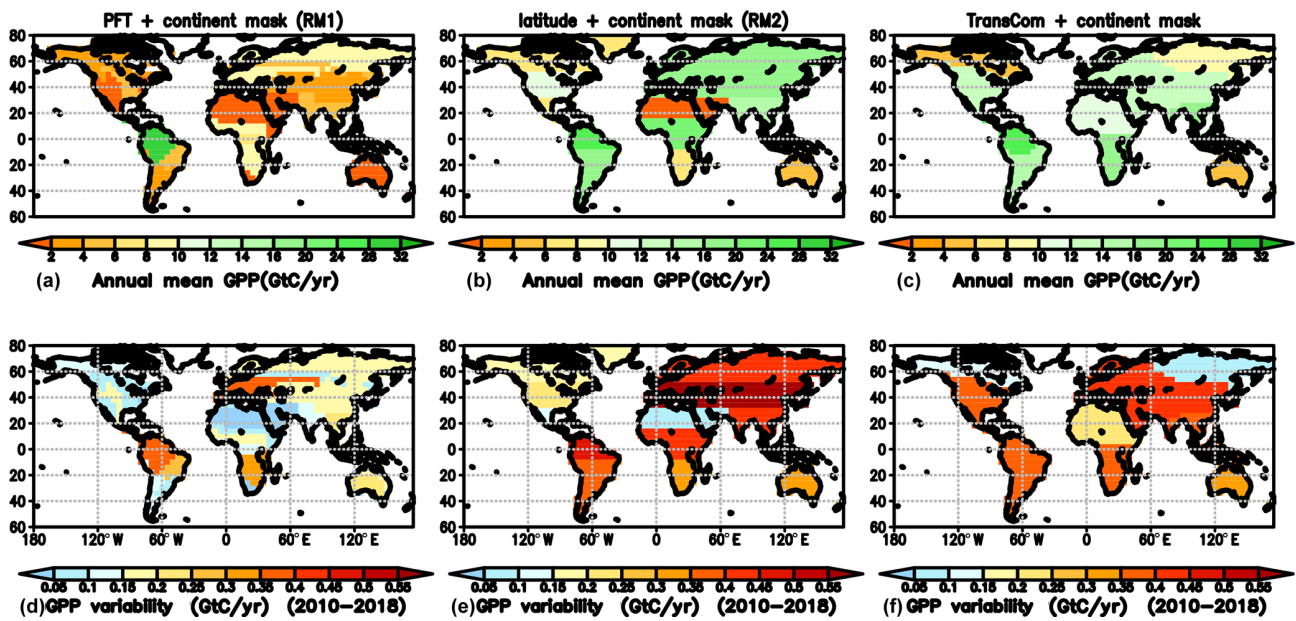
Figure B4. Regional mean FLUXSAT GPP and its variability between 2010–2018. **(a, b, c)** Regional mean GPP aggregated with the three regional masks; **(d, e, f)** GPP variability between 2010–2018. Unit: Gt C/yr.

https://doi.org/10.5194/essd-13-299-2021

Earth Syst. Sci. Data, 13, 299–330, 2021
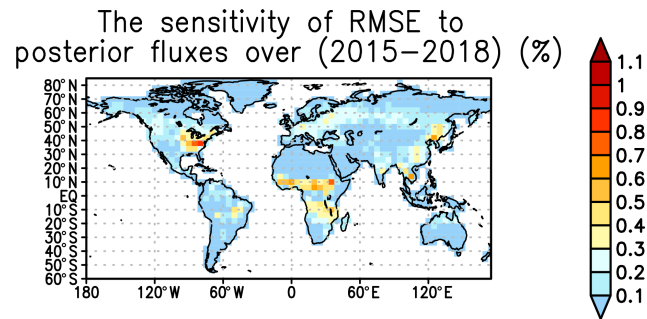
Figure B5. The relative sensitivity of root mean square errors (RMSEs) of posterior CO_2 (Fig. 9 in the main text) relative to NBE at every grid point. The adjoint model is carried out over September 2014–December 2018.
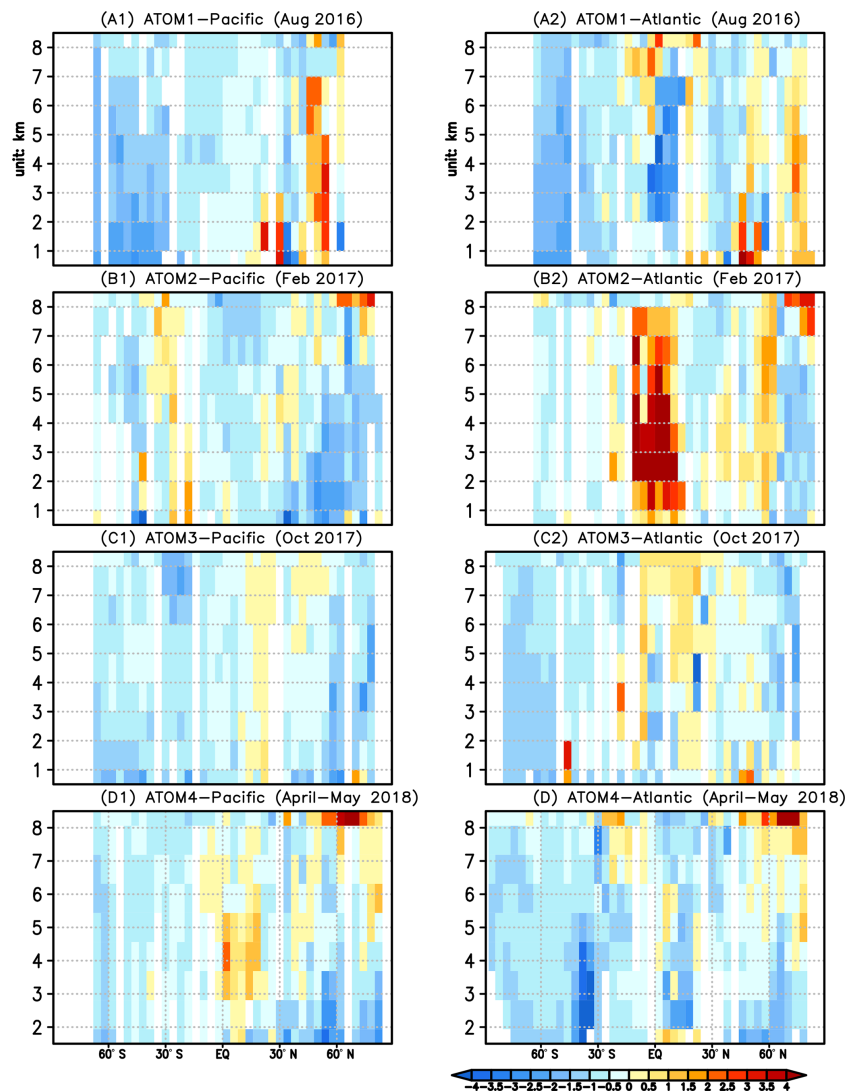
Figure B6. Differences between posterior CO_2 and ATom 1–4 aircraft CO_2 observations over the Pacific (**A1–D1**) and Atlantic Ocean (**A2–D2**) as a function of latitude and altitude (unit: km). Unit: ppm.

Earth Syst. Sci. Data, 13, 299–330, 2021

https://doi.org/10.5194/essd-13-299-2021
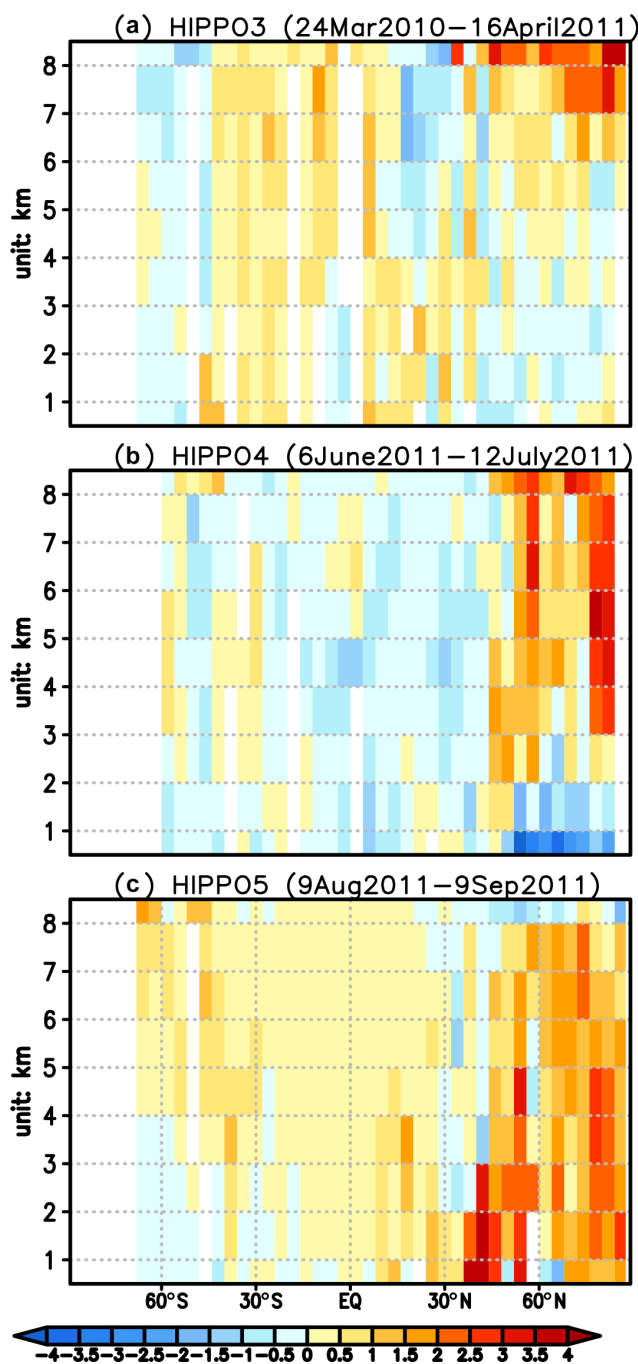
Figure B7. Differences between posterior CO_2 and HIPPO 3–5 aircraft CO_2 observations over the Pacific **(A–C)** as a function of latitude and altitude. Unit: ppm.

https://doi.org/10.5194/essd-13-299-2021

Earth Syst. Sci. Data, 13, 299–330, 2021

(a) Relative sensitivity of RMSE between 40°W−0, 20°S−20°N (ATOM−1) to posterior fluxes (June2016−August2016)
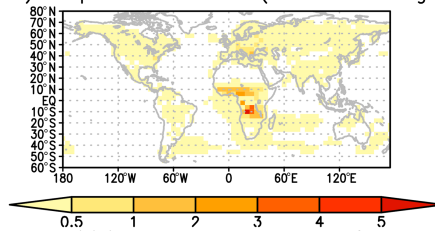
(b) Relative sensitivity of RMSE between 40°W−0, 20°S−20°N (ATOM−2) to posterior fluxes (Dec2016−Feb2017)
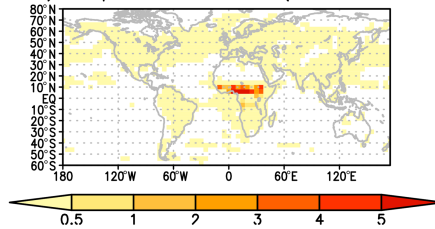
Figure B8. The relative sensitivity of RMSE of posterior CO_2 to NBE over land and air–sea net carbon exchange over ocean at every grid point. The RMSE is calculated against aircraft CO_2 observations from ATom 1 **(a)** and ATom 2 **(b)** between 40° W–0°, 20° S–20° N. The adjoint model is carried out over June–August 2016 **(a)** and December 2016–February 2017 **(b)**. Unit: %.

Relative sensitivity of RMSE between 175°W−20°W, 80°S−30°S (ATOM−1) to posterior fluxes (June−August)
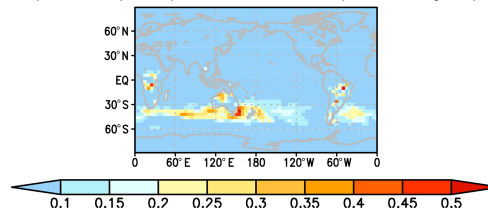
Figure B9. The relative sensitivity of RMSE of posterior CO_2 to NBE over land and air–sea net carbon exchange over ocean at every grid point. The RMSE is calculated against aircraft CO_2 observations from ATom 1 between 175–20° W, 80–30° S. The adjoint model is carried out over June–August 2016. Unit: %.

Relative sensitivity of RMSE between 180°W−130°W, 50°N−90°N (HIPPO−4) to posterior fluxes (Apr−July)
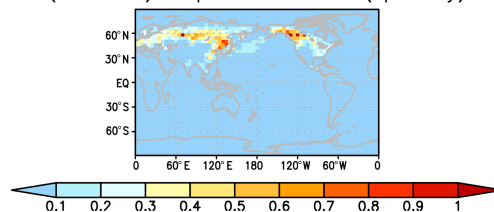
Figure B10. The relative sensitivity of RMSE of posterior CO_2 to NBE over land and air–sea net carbon exchange over ocean at every grid point. The RMSE is calculated against aircraft CO_2 observations from HIPPO 4 between 180–130° W, 50–90° N. The adjoint model is carried out over April–July 2011. Unit: %.
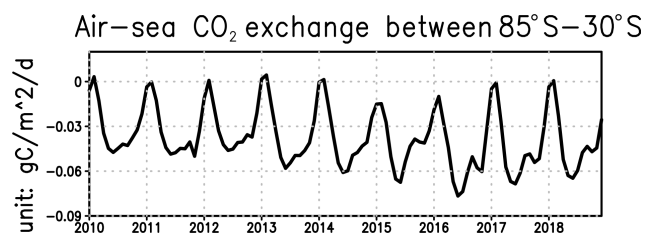
Figure B11. Monthly posterior air–sea CO_2 exchanges between 85–30° S. Unit: $\mathrm{g\,C/m^2/d}$.

References

Arellano Jr., A. F., Kasibhatla, P. S., Giglio, L., Van der Werf, G. R., Randerson, J. T., and Collatz, G. J.: Time-dependent inversion estimates of global biomass-burning CO emissions using Measurement of Pollution in the Troposphere (MO-PITT) measurements, J. Geophys. Res.-Atmos., 111, D09303, https://doi.org/10.1029/2005JD006613, 2006.

Baker, D. F., Doney, S. C., and Schimel, D. S.: Variational data assimilation for atmospheric CO_2, Tellus B, 58, 359–365, https://doi.org/10.1111/j.1600-0889.2006.00218.x, 2006a.

Baker, D. F., Law, R. M., Gurney, K. R., Rayner, P., Peylin, P., Denning, A. S., Bousquet, P., Bruhwiler, L., Chen, Y. H., Ciais, P., and Fung, I. Y.: TransCom 3 inversion intercomparison: Impact of transport model errors on the interannual variability of regional CO_2 fluxes, 1988–2003, Global Biogeochem. Cy., 20, GB1002, https://doi.org/10.1029/2004GB002439, 2006b.

Bastos, A., Friedlingstein, P., Sitch, S., Chen, C., Mialon, A., Wigneron, J.-P., Arora, V. K., Briggs, P. R., Canadell, J. G., and Ciais, P.: Impact of the 2015/2016 El Niño on the terrestrial carbon cycle constrained by bottom-up and top-down approaches, Philos. T. R. Soc. Lond. B., 373, 1760, https://doi.org/10.1098/rstb.2017.0304, 2018.

Bloom, A. A., Exbrayat, J. F., van der Velde, I. R., Feng, L., and Williams, M.: The decadal state of the terrestrial carbon cycle: Global retrievals of terrestrial carbon allocation, pools, and residence times, P. Natl. Acad. Sci. USA, 113, 1285–1290, 2016.

Bloom, A. A., Bowman, K. W., Liu, J., Konings, A. G., Worden, J. R., Parazoo, N. C., Meyer, V., Reager, J. T., Worden, H. M., Jiang, Z., Quetin, G. R., Smallman, T. L., Exbrayat, J.-F., Yin, Y., Saatchi, S. S., Williams, M., and Schimel, D. S.: Lagged effects regulate the inter-annual variability of the tropical carbon balance, Biogeosciences, 17, 6393–6422, https://doi.org/10.5194/bg-17-6393-2020, 2020.

Bowman, K. W., Liu, J., Bloom, A. A., Parazoo, N. C., Lee, M., Jiang, Z., Menemenlis, D., Gierach, M. M., Collatz, G. J., Gurney, K. R., and Wunch, D.: Global and Brazilian carbon response to El Niño Modoki 2011–2010, Earth Space Sci., 4, 637–660, https://doi.org/10.1002/2016EA000204, 2017.

Brix, H., Menemenlis, D., Hill, C., Dutkiewicz, S., Jahn, O., Wang, D., Bowman, K., and Zhang, H.: Using Green's Functions to initialize and adjust a global, eddying ocean biogeochemistry general circulation model, Ocean Model., 95, 1–14, https://doi.org/10.1016/j.ocemod.2015.07.008, 2015.

Byrd, R. H., Nocedal, J., and Schnabel, R. B.: Representations of quasi-Newton matrices and their use in limited memory methods, Math. Program., 63, 129–156, https://doi.org/10.1007/BF01582063, 1994.

Byrne, B., Liu, J., Lee, M., Baker, I., Bowman, K. W., Deutscher, N. M., Feist, D. G., Griffith, D. W. T., Iraci, L. T., Kiel, M., Kimball, J. S., Miller, C. E., Morino, I., Parazoo, N. C., Petri, C. C., Roehl, M., Sha, M. K., Strong, K., Velazco, V. A., Wennberg, P. O., and Wunch, D.: Improved constraints on northern extratropical CO_2 fluxes obtained by combining surface-based and space-based atmospheric CO_2 measurements, J. Geophys. Res.-Atmos., 125, e2019JD032029, https://doi.org/10.1029/2019JD032029, 2020.

Carbontracker Team: Compilation of near real time atmospheric carbon dioxide data; obspack_co2_1_NRT_v5.0_2019-08-13; NOAA Earth System Research Laboratory, Global Monitoring Division, https://doi.org/10.25925/20190813, 2019.

Carroll, D., Menemenlis, D., Adkins, J. F., Bowman, K. W., Brix, H., Dutkiewicz, S., Fenty, I., Gierach, M. M., Hill, C., Jahn, O., Landschützer, P., Lauderdale, J. M., Liu, J., Manizza, M., Naviaux, J. D., Rödenbeck, C., Schimel, D. S., Van der Stocken, T., and Zhang, H.: The ECCO-Darwin Data-assimilative Global Ocean Biogeochemistry Model: Estimates of Seasonal to Multi-decadal Surface Ocean pCO$_2$ and Air-sea

CO_2 Flux, J. Adv. Model. Earth Syst., 12, e2019MS001888, https://doi.org/10.1029/2019MS001888, 2020.

Chevallier, F., Fisher, M., Peylin, P., Serrar, S., Bousquet, P., Bréon, F.M., Chédin, A., and Ciais, P.: Inferring CO_2 sources and sinks from satellite observations: Method and application to TOVS data, J. Geophys. Res.-Atmos., 110, D24309, https://doi.org/10.1029/2005JD006390, 2005.

Chevallier, F., Ciais, P., Conway, T. J., Aalto, T., Anderson, B. E., Bousquet, P., Brunke, E. G., Ciattaglia, L., Esaki, Y., Fröhlich, M., and Gomez, A.: CO_2 surface fluxes at grid point scale estimated from a global 21 year reanalysis of atmospheric measurements, J. Geophys. Res., 115, D21307, https://doi.org/10.1029/2010JD013887, 2010.

Chevallier, F., Remaud, M., O'Dell, C. W., Baker, D., Peylin, P., and Cozic, A.: Objective evaluation of surface- and satellite-driven carbon dioxide atmospheric inversions, Atmos. Chem. Phys., 19, 14233–14251, https://doi.org/10.5194/acp-19-14233-2019, 2019.

Ciais, P., Tan, J., Wang, X., Roedenbeck, C., Chevallier, F., Piao, S. L., Moriarty, R., Broquet, G., Le Quéré, C., Canadell, J. G., and Peng, S.: Five decades of northern land carbon uptake revealed by the interhemispheric CO 2 gradient, Nature, 568, 221–225, https://doi.org/10.1038/s41586-019-1078-6, 2019.

Conway, T. J., Tans, P. P., Waterman, L. S., Thoning, K. W., Kitzis, D. R., Masarie, K. A., and Zhang, N.: Evidence for interannual variability of the carbon cycle from the National Oceanic and Atmospheric Administration/Climate Monitoring and Diagnostics Laboratory Global Air Sampling Network, J. Geophys. Res., 99, 22831–22855, https://doi.org/10.1029/94JD01951, 1994.

Crisp, D., Fisher, B. M., O'Dell, C., Frankenberg, C., Basilio, R., Bösch, H., Brown, L. R., Castano, R., Connor, B., Deutscher, N. M., Eldering, A., Griffith, D., Gunson, M., Kuze, A., Mandrake, L., McDuffie, J., Messerschmidt, J., Miller, C. E., Morino, I., Natraj, V., Notholt, J., O'Brien, D. M., Oyafuso, F., Polonsky, I., Robinson, J., Salawitch, R., Sherlock, V., Smyth, M., Suto, H., Taylor, T. E., Thompson, D. R., Wennberg, P. O., Wunch, D., and Yung, Y. L.: The ACOS $CO2$ retrieval algorithm – Part II: Global XCO_2 data characterization, Atmos. Meas. Tech., 5, 687–707, https://doi.org/10.5194/amt-5-687-2012, 2012.

Crisp, D., Pollock, H. R., Rosenberg, R., Chapsky, L., Lee, R. A. M., Oyafuso, F. A., Frankenberg, C., O'Dell, C. W., Bruegge, C. J., Doran, G. B., Eldering, A., Fisher, B. M., Fu, D., Gunson, M. R., Mandrake, L., Osterman, G. B., Schwandner, F. M., Sun, K., Taylor, T. E., Wennberg, P. O., and Wunch, D.: The on-orbit performance of the Orbiting Carbon Observatory-2 (OCO-2) instrument and its radiometrically calibrated products, Atmos. Meas. Tech., 10, 59–81, https://doi.org/10.5194/amt-10-59-2017, 2017.

Crowell, S., Baker, D., Schuh, A., Basu, S., Jacobson, A. R., Chevallier, F., Liu, J., Deng, F., Feng, L., McKain, K., Chatterjee, A., Miller, J. B., Stephens, B. B., Eldering, A., Crisp, D., Schimel, D., Nassar, R., O'Dell, C. W., Oda, T., Sweeney, C., Palmer, P. I., and Jones, D. B. A.: The 2015–2016 carbon cycle as seen from OCO-2 and the global in situ network, Atmos. Chem. Phys., 19, 9797–9831, https://doi.org/10.5194/acp-19-9797-2019, 2019.

Davis, K. J., Obland, M. D., Lin, B., Lauvaux, T., O'Dell, C., Meadows, B., Browell, E. V., DiGangi, J. P., Sweeney, C., McGill, M. J., Barrick, J. D., Nehrir, A. R., Yang, M. M., Bennett, J. R., Baier, B. C., Roiger, A., Pal, S., Gerken, T., Fried, A., Feng, S., Shrestha, R., Shook, M. A., Chen, G., Camp-

bell, L. J., Barkley, Z. R., and Pauly, R. M.: ACT-America: L3 Merged In Situ Atmospheric Trace Gases and Flask Data, Eastern USA, ORNL DAAC, Oak Ridge, Tennessee, USA, https://doi.org/10.3334/ORNLDAAC/1593, 2018.

Falk, M., Wharton, S., Schroeder, M., Ustin, S., and Paw, U, K. T. P.: Flux partitioning in an old-growth forest: seasonal and interannual dynamics, Tree Physiol., 28, 509–520, https://doi.org/10.1093/treephys/28.4.509, 2008.

Fisher, M. and Courtier, P.: Estimating the covariance matrices of analysis and forecast error in variational data assimilation, Technical Memorandum 220, ECMWF, Reading, UK, 1995.

Friedlingstein, P., Jones, M. W., O'Sullivan, M., Andrew, R. M., Hauck, J., Peters, G. P., Peters, W., Pongratz, J., Sitch, S., Le Quéré, C., Bakker, D. C. E., Canadell, J. G., Ciais, P., Jackson, R. B., Anthoni, P., Barbero, L., Bastos, A., Bastrikov, V., Becker, M., Bopp, L., Buitenhuis, E., Chandra, N., Chevallier, F., Chini, L. P., Currie, K. I., Feely, R. A., Gehlen, M., Gilfillan, D., Gkritzalis, T., Goll, D. S., Gruber, N., Gutekunst, S., Harris, I., Haverd, V., Houghton, R. A., Hurtt, G., Ilyina, T., Jain, A. K., Joetzjer, E., Kaplan, J. O., Kato, E., Klein Goldewijk, K., Korsbakken, J. I., Landschützer, P., Lauvset, S. K., Lefèvre, N., Lenton, A., Lienert, S., Lombardozzi, D., Marland, G., McGuire, P. C., Melton, J. R., Metzl, N., Munro, D. R., Nabel, J. E. M. S., Nakaoka, S.-I., Neill, C., Omar, A. M., Ono, T., Peregon, A., Pierrot, D., Poulter, B., Rehder, G., Resplandy, L., Robertson, E., Rödenbeck, C., Séférian, R., Schwinger, J., Smith, N., Tans, P. P., Tian, H., Tilbrook, B., Tubiello, F. N., van der Werf, G. R., Wiltshire, A. J., and Zaehle, S.: Global Carbon Budget 2019, Earth Syst. Sci. Data, 11, 1783–1838, https://doi.org/10.5194/essd-11-1783-2019, 2019.

Gatti, L. V., Gloor, M., Miller, J. B., Doughty, C. E., Malhi, Y., Domingues, L. G., Basso, L. S., Martinewski, A., Correia, C. S. C., Borges, V. F., and Freitas, S.: Drought sensitivity of Amazonian carbon balance revealed by atmospheric measurements, Nature, 506, 76–80, https://doi.org/10.1038/nature12957, 2014.

Gaubert, B., Stephens, B. B., Basu, S., Chevallier, F., Deng, F., Kort, E. A., Patra, P. K., Peters, W., Rödenbeck, C., Saeki, T., Schimel, D., Van der Laan-Luijkx, I., Wofsy, S., and Yin, Y.: Global atmospheric CO_2 inverse models converging on neutral tropical land exchange, but disagreeing on fossil fuel and atmospheric growth rate, Biogeosciences, 16, 117–134, https://doi.org/10.5194/bg-16-117-2019, 2019.

Giglio, L., Randerson, J. T., and van der Werf, G. R.: Analysis of daily, monthly, and annual burned area using the fourth-generation global fire emissions database (GFED4), J. Geophys. Res.-Biogeo., 118, 317–328, https://doi.org/10.1002/jgrg.20042, 2013.

Gurney, K. R., Law, R. M., Denning, A. S., Rayner, P. J., Pak, B. C., Baker, D., Bousquet, P., Bruhwiler, L., Chen, Y. H., Ciais, P., and Fung, I. Y.: Transcom 3 inversion intercomparison: Model mean results for the estimation of seasonal carbon sources and sinks, Global Biogeochem. Cycles, 18, GB1010, https://doi.org/10.1029/2003GB002111, 2004.

Henze, D. K., Hakami, A., and Seinfeld, J. H.: Development of the adjoint of GEOS-Chem, Atmos. Chem. Phys., 7, 2413–2433, https://doi.org/10.5194/acp-7-2413-2007, 2007.

IPCC: Global warming of 1.5 °C. An IPCC Special Report on the impacts of global warming of 1.5 °C above pre-industrial levels and related global greenhouse gas emission pathways, in the

https://doi.org/10.5194/essd-13-299-2021

Earth Syst. Sci. Data, 13, 299–330, 2021

context of strengthening the global response to the threat of climate change, sustainable development, and efforts to eradicate poverty, edited by: Masson-Delmotte, V., Zhai, P., Pörtner, H. O., Roberts, D., Skea, J., Shukla, P. R., Pirani, A., Moufouma-Okia, W., Péan, C., Pidcock, R., Connors, S., Matthews, J. B. R., Chen, Y., Zhou, X., Gomis, M. I., Lonnoy, E., Maycock, T., Tignor, M., and Waterfield, T., in press, 2021.

Jiang, Z., Worden, J. R., Worden, H., Deeter, M., Jones, D. B. A., Arellano, A. F., and Henze, D. K.: A 15-year record of CO emissions constrained by MOPITT CO observations, Atmos. Chem. Phys., 17, 4565–4583, https://doi.org/10.5194/acp-17-4565-2017, 2017.

Joiner, J., Guanter, L., Lindstrot, R., Voigt, M., Vasilkov, A. P., Middleton, E. M., Huemmrich, K. F., Yoshida, Y., and Frankenberg, C.: Global monitoring of terrestrial chlorophyll fluorescence from moderate-spectral-resolution near-infrared satellite measurements: methodology, simulations, and application to GOME-2, Atmos. Meas. Tech., 6, 2803–2823, https://doi.org/10.5194/amt-6-2803-2013, 2013.

Joiner, J., Yoshida, Y., Zhang, Y., Duveiller, G., Jung, M., Lyapustin, A., Wang, Y., and Tucker, C.: Estimation of terrestrial global gross primary production (GPP) with satellite data-driven models and eddy covariance flux data, Remote Sens., 10, 1346, https://doi.org/10.3390/rs10091346, 2018.

Jones, D. B. A., Bowman, K. W., Logan, J. A., Heald, C. L., Liu, J., Luo, M., Worden, J., and Drummond, J.: The zonal structure of tropical O$_3$ and CO as observed by the Tropospheric Emission Spectrometer in November 2004 – Part 1: Inverse modeling of CO emissions, Atmos. Chem. Phys., 9, 3547–3562, https://doi.org/10.5194/acp-9-3547-2009, 2009.

Reichstein, M., Schwalm, C. R., Huntingford, C., Sitch, S., Ahlström, A., Arneth, A., Camps-Valls, G., Ciais, P., Friedlingstein, P., Gans, F., Ichii, K., Jain, A. K., Kato, E., Papale, D., Poulter, B., Raduly, B., Rödenbeck, C., Tramontana, G., Viovy, N., Wang, Y.-P., Weber, U., Zaehle, S., and Zeng, N.: Compensatory water effects link yearly global land CO 2 sink changes to temperature, Nature, 541, 516–520, 2017.

Kiel, M., O'Dell, C. W., Fisher, B., Eldering, A., Nassar, R., MacDonald, C. G., and Wennberg, P. O.: How bias correction goes wrong: measurement of XCO$_2$ affected by erroneous surface pressure estimates, Atmos. Meas. Tech., 12, 2241–2259, https://doi.org/10.5194/amt-12-2241-2019, 2019.

Konings, A. G., Bloom, A. A., Liu, J., Parazoo, N. C., Schimel, D. S., and Bowman, K. W.: Global satellite-driven estimates of heterotrophic respiration, Biogeosciences, 16, 2269–2284, https://doi.org/10.5194/bg-16-2269-2019, 2019.

Kulawik, S. S., Crowell, S., Baker, D., Liu, J., McKain, K., Sweeney, C., Biraud, S. C., Wofsy, S., O'Dell, C. W., Wennberg, P. O., Wunch, D., Roehl, C. M., Deutscher, N. M., Kiel, M., Griffith, D. W. T., Velazco, V. A., Notholt, J., Warneke, T., Petri, C., De Mazière, M., Sha, M. K., Sussmann, R., Rettinger, M., Pollard, D. F., Morino, I., Uchino, O., Hase, F., Feist, D. G., Roche, S., Strong, K., Kivi, R., Iraci, L., Shiomi, K., Dubey, M. K., Sepulveda, E., Rodriguez, O. E. G., Té, Y., Jeseck, P., Heikkinen, P., Dlugokencky, E. J., Gunson, M. R., Eldering, A., Crisp, D., Fisher, B., and Osterman, G. B.: Characterization of OCO-2 and ACOS-GOSAT biases and errors for CO$_2$ flux estimates, Atmos. Meas. Tech. Discuss. [preprint], https://doi.org/10.5194/amt-2019-257, 2019.

Kuze, A., Suto, H., Shiomi, K., Kawakami, S., Tanaka, M., Ueda, Y., Deguchi, A., Yoshida, J., Yamamoto, Y., Kataoka, F., Taylor, T. E., and Buijs, H. L.: Update on GOSAT TANSO-FTS performance, operations, and data products after more than 6 years in space, Atmos. Meas. Tech., 9, 2445–2461, https://doi.org/10.5194/amt-9-2445-2016, 2016.

Le Quéré, C., Andrew, R. M., Friedlingstein, P., Sitch, S., Pongratz, J., Manning, A. C., Korsbakken, J. I., Peters, G. P., Canadell, J. G., Jackson, R. B., Boden, T. A., Tans, P. P., Andrews, O. D., Arora, V. K., Bakker, D. C. E., Barbero, L., Becker, M., Betts, R. A., Bopp, L., Chevallier, F., Chini, L. P., Ciais, P., Cosca, C. E., Cross, J., Currie, K., Gasser, T., Harris, I., Hauck, J., Haverd, V., Houghton, R. A., Hunt, C. W., Hurtt, G., Ilyina, T., Jain, A. K., Kato, E., Kautz, M., Keeling, R. F., Klein Goldewijk, K., Körtzinger, A., Landschützer, P., Lefèvre, N., Lenton, A., Lienert, S., Lima, I., Lombardozzi, D., Metzl, N., Millero, F., Monteiro, P. M. S., Munro, D. R., Nabel, J. E. M. S., Nakaoka, S., Nojiri, Y., Padin, X. A., Peregon, A., Pfeil, B., Pierrot, D., Poulter, B., Rehder, G., Reimer, J., Rödenbeck, C., Schwinger, J., Séférian, R., Skjelvan, I., Stocker, B. D., Tian, H., Tilbrook, B., Tubiello, F. N., van der Laan-Luijkx, I. T., van der Werf, G. R., van Heuven, S., Viovy, N., Vuichard, N., Walker, A. P., Watson, A. J., Wiltshire, A. J., Zaehle, S., and Zhu, D.: Global Carbon Budget 2017, Earth Syst. Sci. Data, 10, 405–448, https://doi.org/10.5194/essd-10-405-2018, 2018.

Liu, J. and Bowman, K.: A method for independent validation of surface fluxes from atmospheric inversion: Application to CO$_2$, Geophys. Res. Lett., 43, 3502–3508, https://doi.org/10.1002/2016GL067828, 2016.

Liu, J., Bowman, K. W., Lee, M., Henze, D. K., Bousserez, N., Brix, H., James Collatz, G., Menemenlis, D., Ott, L., Pawson, S., and Jones, D.: Carbon monitoring system flux estimation and attribution: impact of ACOS-GOSAT XCO$_2$ sampling on the inference of terrestrial biospheric sources and sinks, Tellus B, 66, 22486, https://doi.org/10.3402/tellusb.v66.22486, 2014.

Liu, J., Bowman, K. W., and Henze, D. K.: Source-receptor relationships of column-average CO$_2$ and implications for the impact of observations on flux inversions, J. Geophys. Res.-Atmos., 120, 5214–5236, https://doi.org/10.1002/2014JD022914, 2015.

Liu, J., Bowman, K. W., Schimel, D. S., Parazoo, N. C., Jiang, Z., Lee, M., Bloom, A. A., Wunch, D., Frankenberg, C., Sun, Y., and O'Dell, C. W.: Contrasting carbon cycle responses of the tropical continents to the 2015–2016 El Niño, Science, 358, eaam5690, https://doi.org/10.1126/science.aam5690, 2017.

Liu, J., Bowman, K., Parazoo, N. C., Bloom, A. A., Wunch, D., Jiang, Z., Gurney, K. R., and Schimel, D.: Detecting drought impact on terrestrial biosphere carbon fluxes over contiguous US with satellite observations, Environ. Res. Lett., 13, 095003, https://doi.org/10.1088/1748-9326/aad5ef, 2018.

Liu, J., Baskarran, L., Bowman, K., Schimel, D., Bloom, A. A., Parazoo, N., Oda, T., Carrol, D., Menemenlis, D., Joiner, J., Commane, R., Daube, B., Gatti, L. V., McKain, K., Miller, J., Stephens, B. B., Sweeney, C., and Wofsy, S.: CMS-Flux NBE 2020 [Data set], NASA, https://doi.org/10.25966/4V02-C391, 2020.

Liu, Z.-Q. and Rabier, F.: The potential of high-density observations for numerical weather prediction: A study with simulated observations, Q. J. Roy. Meteor. Soc., 129, 3013–035, https://doi.org/10.1256/qj.02.170, 2003.

Lorenc, A. C.: A Global Three-Dimensional Multivariate Statistical Interpolation Scheme, Mon. Weather Rev., 109, 701–721, 1981.

Lovenduski, N. S. and Bonan, G. B.: Reducing uncertainty in projections of terrestrial carbon uptake, Environ. Res. Lett., 12, 044020, https://doi.org/10.1088/1748-9326/aa66b8, 2017.

Meirink, J. F., Bergamaschi, P., and Krol, M. C.: Four-dimensional variational data assimilation for inverse modelling of atmospheric methane emissions: method and comparison with synthesis inversion, Atmos. Chem. Phys., 8, 6341–6353, https://doi.org/10.5194/acp-8-6341-2008, 2008.

Nassar, R., Jones, D. B. A., Suntharalingam, P., Chen, J. M., Andres, R. J., Wecht, K. J., Yantosca, R. M., Kulawik, S. S., Bowman, K. W., Worden, J. R., Machida, T., and Matsueda, H.: Modeling global atmospheric CO2 with improved emission inventories and CO2 production from the oxidation of other carbon species, Geosci. Model Dev., 3, 689–716, https://doi.org/10.5194/gmd-3-689-2010, 2010.

Niwa, Y. and Fujii, Y.: A conjugate BFGS method for accurate estimation of a posteriori error covariance matrix in a linear inverse problem, Q. J. Roy. Meteor. Soc., 146, 3118–3143, https://doi.org/10.1002/qj.3838, 2020.

Oda, T., Maksyutov, S., and Andres, R. J.: The Open-source Data Inventory for Anthropogenic CO_2, version 2016 (ODIAC2016): a global monthly fossil fuel CO_2 gridded emissions data product for tracer transport simulations and surface flux inversions, Earth Syst. Sci. Data, 10, 87–107, https://doi.org/10.5194/essd-10-87-2018, 2018.

O'Dell, C. W., Connor, B., Bösch, H., O'Brien, D., Frankenberg, C., Castano, R., Christi, M., Eldering, D., Fisher, B., Gunson, M., McDuffie, J., Miller, C. E., Natraj, V., Oyafuso, F., Polonsky, I., Smyth, M., Taylor, T., Toon, G. C., Wennberg, P. O., and Wunch, D.: The ACOS CO2 retrieval algorithm – Part 1: Description and validation against synthetic observations, Atmos. Meas. Tech., 5, 99–121, https://doi.org/10.5194/amt-5-99-2012, 2012.

O'Dell, C. W., Eldering, A., Wennberg, P. O., Crisp, D., Gunson, M. R., Fisher, B., Frankenberg, C., Kiel, M., Lindqvist, H., Mandrake, L., Merrelli, A., Natraj, V., Nelson, R. R., Osterman, G. B., Payne, V. H., Taylor, T. E., Wunch, D., Drouin, B. J., Oyafuso, F., Chang, A., McDuffie, J., Smyth, M., Baker, D. F., Basu, S., Chevallier, F., Crowell, S. M. R., Feng, L., Palmer, P. I., Dubey, M., García, O. E., Griffith, D. W. T., Hase, F., Iraci, L. T., Kivi, R., Morino, I., Notholt, J., Ohyama, H., Petri, C., Roehl, C. M., Sha, M. K., Strong, K., Sussmann, R., Te, Y., Uchino, O., and Velazco, V. A.: Improved retrievals of carbon dioxide from Orbiting Carbon Observatory-2 with the version 8 ACOS algorithm, Atmos. Meas. Tech., 11, 6539–6576, https://doi.org/10.5194/amt-11-6539-2018, 2018.

Olsen, S. C. and Randerson, J. T.: Differences between surface and column atmospheric CO_2 and implications for carbon cycle research, J. Geophys. Res.-Atmos., 109, D02301, https://doi.org/10.1029/2003JD003968, 2004.

Osterman, G., O'Dell, C., and Eldering, A.: Data Product User's Guide, Operational Level 2 Data Versions 10 and Lite File Version 10 and VEarly, available at: https://docserver.gesdisc.eosdis.nasa.gov/public/project/OCO/OCO2_OCO3_B10_DUG.pdf, last access: 10 September 2020.

Parazoo, N. C., Bowman, K., Fisher, J. B., Frankenberg, C., Jones, D. B. A., Cescatti, A., Pérez-Priego, Ó., Wohlfahrt, G., and Montagnani, L.: Terrestrial gross primary production inferred from satellite fluorescence and vegetation models, Global Change Biol., 20, 3103–3121, https://doi.org/10.1111/gcb.12652, 2014.

Peylin, P., Law, R. M., Gurney, K. R., Chevallier, F., Jacobson, A. R., Maki, T., Niwa, Y., Patra, P. K., Peters, W., Rayner, P. J., Rödenbeck, C., van der Laan-Luijkx, I. T., and Zhang, X.: Global atmospheric carbon budget: results from an ensemble of atmospheric CO2 inversions, Biogeosciences, 10, 6699–6720, https://doi.org/10.5194/bg-10-6699-2013, 2013.

Peters, W., Jacobson, A. R., Sweeney, C., Andrews, A. E., Conway, T. J., Masarie, K., Miller, J. B., Bruhwiler, L. M. P., Pétron, G., Hirsch, A. I., Worthy, D. E. J., van der Werf, G. R., Randerson, J. T., Wennberg, P. O., Krol, M. C., and Tans, P. P.: An atmospheric perspective on North American carbon dioxide exchange: CarbonTracker, P. Natl. Acad. Sci. USA, 104, 18925–18930, https://doi.org/10.1073/pnas.0708986104, 2007.

Peters, W., Krol, M. C., Van Der Werf, G. R., Houweling, S., Jones, C. D., Hughes, J., Schaefer, K., Masarie, K. A., Jacobson, A. R., Miller, J. B., Cho, C. H., Ramonet, M., Schmidt, M., Ciattaglia, L., Apadula, F., Heltai, D., Meinhardt, F., Di Sarra, A. G., Piacentino, S., Sferlazzo, D., Aalto, T., Hatakka, J., Ström, J., Haszpra, L., Meijer, H. A. J., Van Der Laan, S., Neubert, R. E. M., Jordan, A., Rodó, X., Morguí, J.-A., Vermeulen, A. T., Popa, E., Rozanski, K., Zimnoch, M., Manning, A. C., Leuenberger, M., Uglietti, C., Dolman, A. J., Ciais, P., Heimann, M., and Tans, P. P.: Seven years of recent European net terrestrial carbon dioxide exchange constrained by atmospheric observations, Global Change Biol., 16, 1317–1337, https://doi.org/10.1111/j.1365-2486.2009.02078.x, 2010.

Poulter, B., Frank, D., Ciais, P., Myneni, R. B., Andela, N., Bi, J., Broquet, G., Canadell, J. G., Chevallier, F., Liu, Y. Y., and Running, S. W.: Contribution of semi-arid ecosystems to interannual variability of the global carbon cycle, Nature, 509, 600–603, https://doi.org/10.1038/nature13376, 2014.

Quetin, G., Bloom, A. A., Bowman, K. W., and Konings, A.: Carbon flux variability from a relatively simple ecosystem model with assimilated data is consistent with terrestrial biosphere model estimates, J. Adv. Model. Earth Syst., 12, e2019MS001889, https://doi.org/10.1029/2019MS001889, 2020.

Randerson, J. T., Van Der Werf, G. R., Giglio, L., Collatz, G. J., and Kasibhatla, P. S.: Global Fire Emissions Database, Version 4.1 (GFEDv4), ORNL DAAC, Oak Ridge, Tennessee, USA, https://doi.org/10.3334/ORNLDAAC/1293, 2018.

Rienecker, M. M., Suarez, M. J., Todling, R., Bacmeister, J., Takacs, L., Liu, H.-C., Gu, W., Sienkiewicz, M., Koster, R. D., Gelaro, R., Stajner, I., and Nielsen, E.: 92. The GEOS-5 Data Assimilation System-Documentation of versions 5.0.1 and 5.1.0, and 5.2.0, NASA Tech. Rep. Series on Global Modeling and Data Assimilation, NASA/TM-2008-104606, vol. 27, 2008.

Rödenbeck, C., Houweling, S., Gloor, M., and Heimann, M.: CO2 flux history 1982–2001 inferred from atmospheric data using a global inversion of atmospheric transport, Atmos. Chem. Phys., 3, 1919–1964, https://doi.org/10.5194/acp-3-1919-2003, 2003.

Running, S. W., Baldocchi, D. D., Turner, D. P., Gower, S. T., Bakwin, P. S., and Hibbard, K. A.: A global terrestrial monitoring network integrating tower fluxes, flask sampling, ecosystem modeling and EOS satellite data, Remote Sens. Environ., 70, 108–127, https://doi.org/10.1016/S0034-4257(99)00061-9, 1999.

Schuh, A. E., Jacobson, A. R., Basu, S., Weir, B., Baker, D., Bowman, K., Chevallier, F., Crowell, S., Davis, K. J., Deng, F., and Denning, S.: Quantifying the impact of atmospheric transport uncertainty on CO_2 surface flux estimates, Global Biogeochem. Cy., 33, 484–500, https://doi.org/10.1029/2018GB006086, 2019.

Sellers, P. J., Schimel, D. S., Moore, B., Liu, J., and Eldering, A.: Observing carbon cycle–climate feedbacks from space, P. Natl. Acad. Sci. USA, 115, 7860–7868, https://doi.org/10.1073/pnas.1716613115, 2018.

Stephens, B., Bent, J., Watt, A., Keeling, R., Morgan, E., and Afshar, S.: ORCAS Airborne Oxygen Instrument. Version 1.0. UCAR/NCAR – Earth Observing Laboratory, https://doi.org/10.5065/D6N29VC6, 2017.

Stephens, B. B., Gurney, K. R., Tans, P. P., Sweeney, C., Peters, W., Bruhwiler, L., Ciais, P., Ramonet, M., Bousquet, P., Nakazawa, T., Aoki, S., Machida, T., Inoue, G., Vinnichenko, N., Lloyd, J., Jordan, A., Heimann, M., Shibistova, O., Langenfelds, R. L., Steele, L. P., Francey, R. J., and Denning, A. S.: Weak northern and strong tropical land carbon uptake from vertical profiles of atmospheric CO_2, Science, 316, 1732–1735, https://doi.org/10.1126/science.1137004, 2007.

Suntharalingam, P., Jacob, D. J., Palmer, P. I., Logan, J. A., Yantosca, R. M., Xiao, Y., Evans, M. J., Streets, D. G., Vay, S. L., and Sachse, G. W.: Improved quantification of Chinese carbon fluxes using CO_2 / CO correlations in Asian outflow, J. Geophys. Res.-Atmos., 109, D18S18, https://doi.org/10.1029/2003JD004362, 2004.

Sweeney, C., Karion, A., Wolter, S., Newberger, T., Guenther, D., Higgs, J. A., Andrews, A. E., Lang, P. M., Neff, D., Dlugokencky, E., Miller, J. B., Montzka, S. A., Miller, B. R., Masarie, K. A., Biraud, S. C., Novelli, P. C., Crotwell, M., Crotwell, A. M., Thoning, K., and Tans, P. P.: Seasonal climatology of CO_2 across North America from aircraft measurements in the NOAA/ESRL Global Greenhouse Gas Reference Network, J. Geophys. Res.-Atmos., 120, 5155–5190, https://doi.org/10.1002/2014JD022591, 2015.

Tramontana, G., Jung, M., Schwalm, C. R., Ichii, K., Camps-Valls, G., Ráduly, B., Reichstein, M., Arain, M. A., Cescatti, A., Kiely, G., Merbold, L., Serrano-Ortiz, P., Sickert, S., Wolf, S., and Papale, D.: Predicting carbon dioxide and energy fluxes across global FLUXNET sites with regression algorithms, Biogeosciences, 13, 4291–4313, https://doi.org/10.5194/bg-13-4291-2016, 2016.

van der Laan-Luijkx, I. T., van der Velde, I. R., van der Veen, E., Tsuruta, A., Stanislawska, K., Babenhauserheide, A., Zhang, H. F., Liu, Y., He, W., Chen, H., Masarie, K. A., Krol, M. C., and Peters, W.: The CarbonTracker Data Assimilation Shell (CTDAS) v1.0: implementation and global carbon balance 2001–2015, Geosci. Model Dev., 10, 2785–2800, https://doi.org/10.5194/gmd-10-2785-2017, 2017.

van der Werf, G. R., Randerson, J. T., Giglio, L., Gobron, N., and Dolman, A. J.: Climate controls on the variability of fires in the tropics and subtropics, Global Biogeochem. Cycles, 22, GB3028, https://doi.org/10.1029/2007GB003122, 2008.

Wofsy, S. C.: HIAPER Pole-to-Pole Observations (HIPPO): Fine-grained, global-scale measurements of climatically important atmospheric gases and aerosols, Philos. T. R. Soc. A, 369, 2073–2086, https://doi.org/10.1098/rsta.2010.0313, 2011.

Wofsy, S. C., Afshar, S., Allen, H. M., Apel, E., Asher, E. C., Barletta, B., Bent, J., Bian, H., Biggs, B. C., Blake, D. R., and Blake, N.: ATom: Merged Atmospheric Chemistry, Trace Gases, and Aerosols, ORNL DAAC, Oak Ridge, Tennessee, USA, https://doi.org/10.3334/ORNLDAAC/1581, 2018.

Wunch, D., Toon, G. C., Blavier, J. F. L., Washenfelder, R. A., Notholt, J., Connor, B. J., Griffith, D. W., Sherlock, V., and Wennberg, P. O.: The total carbon column observing network, Philos. T. R. Soc. A, 369, 2087–2112, https://doi.org/10.1098/rsta.2010.0240, 2011.

Yin, Y., Bowman, K., Bloom, A. A., and Worden, J.: Detection of fossil fuel emission trends in the presence of natural carbon cycle variability, Environ. Res. Lett., 14, 084050, https://doi.org/10.1088/1748-9326/ab2dd7, 2019.

Zhu, C., Byrd, R. H., Lu, P., and Nocedal, J.: Algorithm 778: L-BFGS-B: Fortran subroutines for large-scale bound-constrained optimization, ACM Trans. Math. Softw., 23, 550–560, https://doi.org/10.1145/279232.279236, 1997.